Check for updates

JGR Space Physics

RESEARCH ARTICLE
10.1029/2023JA032234

Density and Magnetic Field Asymmetric Kelvin-Helmholtz Instability

Xuanye Ma[1], Peter Delamere[2], Katariina Nykyri[1], Antonius Otto[2], Stefan Eriksson[3], Lihui Chai[4], Brandon Burkholder[5,6], Andrew Dimmock[7], Yu-Lun Liou[1], and Shiva Kavosi[1]

[1]Embry-Riddle Aeronautical University, Daytona Beach, FL, USA, [2]University of Alaska Fairbanks, Fairbanks, AK, USA, [3]University of Colorado Boulder, Boulder, CO, USA, [4]Institute of Geology and Geophysics, Fairbanks, AK, USA, [5]University of Maryland, Baltimore, MD, USA, [6]NASA Goddard Space Flight Center, Greenbelt, MD, USA, [7]Swedish Institute of Space Physics, Uppsala, Sweden

Key Points:

- The growth of Kelvin-Helmholtz (KH) instability is not sensitive to the density asymmetry
- Magnetic field asymmetry affects KH instability differently during northward and southward interplanetary magnetic field (IMF) conditions
- Different ion velocity distributions can be generated during northward IMF conditions

Correspondence to:
X. Ma,
max@erau.edu

Citation:
Ma, X., Delamere, P., Nykyri, K., Otto, A., Eriksson, S., Chai, L., et al. (2024). Density and magnetic field asymmetric Kelvin-Helmholtz instability. *Journal of Geophysical Research: Space Physics*, *129*, e2023JA032234. https://doi.org/10.1029/2023JA032234

Received 26 OCT 2023
Accepted 20 FEB 2024

© 2024 The Authors.
This is an open access article under the terms of the Creative Commons Attribution-NonCommercial License, which permits use, distribution and reproduction in any medium, provided the original work is properly cited and is not used for commercial purposes.

Abstract The Kelvin-Helmholtz (KH) instability can transport mass, momentum, magnetic flux, and energy between the magnetosheath and magnetosphere, which plays an important role in the solar-wind-magnetosphere coupling process for different planets. Meanwhile, strong density and magnetic field asymmetry are often present between the magnetosheath (MSH) and magnetosphere (MSP), which could affect the transport processes driven by the KH instability. Our magnetohydrodynamics simulation shows that the KH growth rate is insensitive to the density ratio between the MSP and the MSH in the compressible regime, which is different than the prediction from linear incompressible theory. When the interplanetary magnetic field (IMF) is parallel to the planet's magnetic field, the nonlinear KH instability can drive a double mid-latitude reconnection (DMLR) process. The total double reconnected flux depends on the KH wavelength and the strength of the lower magnetic field. When the IMF is anti-parallel to the planet's magnetic field, the nonlinear interaction between magnetic reconnection and the KH instability leads to fast reconnection (i.e., close to Petschek reconnection even without including kinetic physics). However, the peak value of the reconnection rate still follows the asymmetric reconnection scaling laws. We also demonstrate that the DMLR process driven by the KH instability mixes the plasma from different regions and consequently generates different types of velocity distribution functions. We show that the counter-streaming beams can be simply generated via the change of the flux tube connection and do not require parallel electric fields.

1. Introduction

The Kelvin-Helmholtz (KH) instability is driven by a large sheared flow (Chandrasekhar, 1961), which is an important physical mechanism for the viscous-like interaction between the Earth's magnetosphere (MSP) and the solar wind (SW) (Axford, 1964; Axford & Hines, 1961). There are lots of in-situ observation events during both north- and southward interplanetary magnetic field (IMF) conditions at low-latitudes (Blasl et al., 2022; Eriksson, Lavraud, et al., 2016; Henry et al., 2017; Hwang et al., 2011; Kavosi et al., 2023; Li et al., 2013, 2016, 2023; Rice et al., 2022; Wilder et al., 2023; Yan et al., 2014, 2022), as well as at high latitudes with IMF mostly along the dawn or dusk direction (Hwang et al., 2012; Ma et al., 2016; Nykyri et al., 2021). Kavosi and Raeder (2015) shows that for Earth's magnetopause, KH waves occur about 19% of the time. About 35% were for near northward IMF, about 20% for radial or quasi-radial IMF, and only about 10% for southward IMF. It has also been shown that the KH instability can occur at Mercury (Paral & Rankin, 2013), Venus (Dang et al., 2022; Pope et al., 2009; Walker et al., 2011), Mars (Poh et al., 2021), Jupiter (B. Zhang et al., 2018; Ma et al., 2022; Desroche et al., 2012), and Saturn (Desroche et al., 2013; Ma et al., 2015; Masters et al., 2012), as well as in the solar corona (Foullon et al., 2011, 2013; Nykyri & Foullon, 2013; Ofman & Thompson, 2011).

Assuming an infinitely thin sheared flow boundary, Chandrasekhar (1961) demonstrated that the KH growth rate, γ, for an incompressible magnetohydrodynamics (MHD) system is given by

$$\gamma = \sqrt{\alpha_1\alpha_2[(\mathbf{u}_1 - \mathbf{u}_2)\cdot\mathbf{k}]^2 - \alpha_1(\mathbf{u}_{A1}\cdot\mathbf{k})^2 - \alpha_2(\mathbf{u}_{A2}\cdot\mathbf{k})^2}, \quad (1)$$

where the subscripts 1 and 2 represent the value on each side of the sheared flow boundary layer, $\alpha_i = \rho_i/(\rho_1+\rho_2)$, ρ is the mass density, $\mathbf{u}$ is the bulk velocity, $\mathbf{u}_A = \mathbf{B}/\sqrt{\mu_0\rho}$ is the Alfvén velocity, $\mathbf{B}$ is the magnetic field, μ_0 is the

21699402, 2024, 3, Downloaded from https://agupubs.onlinelibrary.wiley.com/doi/10.1029/2023JA032234, Wiley Online Library on [17/05/2024]. See the Terms and Conditions (https://onlinelibrary.wiley.com/terms-and-conditions) on Wiley Online Library for rules of use; OA articles are governed by the applicable Creative Commons License

vacuum permeability, **k** is KH wave-vector. Equation 1 reveals that a large flow shear can increase the KH growth rate and the magnetic field in the KH wave-vector direction can stabilize the KH instability. Equation 1 also indicates that a large density ratio between the magnetosheath (MSH) and the magnetosphere can reduce the KH growth rate.

It is important to notice that for heliophysical objects there is often a large density asymmetry or magnetic field asymmetry across the sheared flow layer. For instance, the typical Earth's magnetosheath number density is about 10 times larger than the magnetospheric number density, while the magnetosheath and magnetospheric magnetic fields are comparable (Ma et al., 2020). However, if a plasmaspheric plume reaches the magnetopause, the magnetospheric number density will be comparable to or even larger than the magnetosheath number density (Walsh et al., 2015). The typical number density ratio across Venus' ionopause boundary is about 100 to 1,000, while there is no or weak magnetic field in Venus' ionosphere (Möstl et al., 2011). For Mars and Saturn, the magnetosheath number density is about 10 times greater than the magnetospheric number density. However, the ion population in the magnetosphere is much heavier than the proton, which leads to the mass densities being comparable across the sheared flow layer (Delamere et al., 2013; Poh et al., 2021). These large density or magnetic field asymmetries (and consequently temperature asymmetry) affect the growth of the KH waves as well as the secondary instabilities (e.g., magnetic reconnection).

At the Earth's magnetopause during the northward IMF condition, the large vortices driven by the nonlinear KH instability can drag low-latitude magnetosheath magnetic field lines in the sun-ward direction and low-latitude magnetospheric magnetic field lines in the tail-ward direction, reminiscent of a “candy wrapper.” This process can generate strong anti-parallel magnetic field components at mid-latitude and consequently trigger a pair of mid-latitude reconnection sites, which is often referred to as double-mid-latitude-reconnection (DMLR) (Eriksson et al., 2021; Faganello et al., 2012; Otto, 2006). The net effect of this DMLR process exchanges the low-latitude magnetosheath and magnetospheric flux tubes, which provides a net mass transport from the magnetosheath into the magnetosphere (Ma et al., 2017). It is expected that such a scenario can also occur at Venus' ionopause boundary layer as the ion escape mechanism. The presence of heavy ions with a weak magnetic field on the ionospheric side is likely to increase the mass transport rate. However, strong density asymmetry is likely to reduce the KH growth rate and the weak magnetic field is expected to limit plausibly exchangeable magnetic flux. Thus, it is interesting to explore the influence of large density and magnetic field asymmetry on the mass transport rate. Meanwhile, the DMLR at the Earth's magnetopause also indicates the mixing of plasma with different temperatures, which is expected to generate different types of velocity distribution functions (VDFs).

In the case of strong magnetic asymmetry, the DMLR process can generate magnetic bottle structures. Both bottle-body (i.e., the weaker magnetic field region) and bottle-neck (i.e., the stronger magnetic field region) for newly reconnected magnetic field lines can be present in the vicinity of the equatorial plane. It is, therefore, interesting to examine whether charged particles can be trapped or accelerated in this structure. Previous simulations and observations have shown that particles can be effectively accelerated in magnetic bottle structures created by magnetic reconnection at high latitudes (diamagnetic cavities) (Burkholder et al., 2020; Kavosi et al., 2018; Nykyri et al., 2012, 2019).

At the Earth's magnetopause during the southward IMF condition, both the KH instability and magnetic reconnection can operate simultaneously (Ma et al., 2014a, 2014b). A fast reconnection rate (i.e., Petschek reconnection rate) can be achieved even without including kinetic physics due to the fast expansion of the x-line. However, the total open flux is limited, since the KH instability diffuses the large-scale current sheet. A strong magnetic field asymmetry is expected to decrease the reconnection rate due to the lower magnetic field strength at one side which lowers the Alfvén speed. Thus, it is interesting to explore whether the asymmetric reconnection rate influenced by the KH instability can still reach the Petschek reconnection rate.

In this paper, we will mainly use numerical MHD simulations as well as test particle simulations to explore the influence of density asymmetry and magnetic asymmetry on KH instability. Section 2 will roughly describe the numerical methods used in this study, the main simulation results will be presented in Sections 3 and 4. We will discuss the application of these results in Section 5. The main results will be summarized in Section 6.

Table 1
List of Values of Free Parameters for Each Case

	ρ_1	ρ_2	B_1	B_2	Region 1	Region 2
2D	$4/(N+1)$	$4\ N/(N+1)$	1	1	MSP	MSH
N-D	2.5	0.25	1	1	MSH	MSP
N-M1	1	1	1	1	MSH	MSP
N-M2	1	1	1	0.5	MSH	MSP
N-M3	1	2.78	1.5	0.5	MSH	MSP
S-M1	1	1	1	−1	MSP	MSH
S-M2	1	1	1	−0.5	MSP	MSH
S-M3	1	1	1.5	−0.5	MSP	MSH

2. Methods

2.1. MHD Simulation

The MHD KH instability is numerically simulated by solving a full set of normalized resistive MHD equations using a leap-frog scheme in a Cartesian coordinate system (Ma et al., 2014a, 2017, 2019; Nykyri & Otto, 2001; Otto & Fairfield, 2000). All physical quantities are normalized by their normalization values, which are given by length scale $L_0 = 640$ km, number density $n_0 = 10\ \mathrm{cm}^{-3}$, the mass density is $\rho_0 = m_p n_0$, where $m_p = 1.67 \times 10^{-27}$ kg is the proton mass, magnetic field magnitude $B_0 = 70$ nT, and the normalization value of other quantities can be derived from these three quantities. These parameters are chosen to be close to the MMS KH event observed by Eriksson, Lavraud, et al. (2016), which is only used for the test particle simulations. All MHD results do not depend on these normalization values. For all simulations, the x direction is the normal direction of the unperturbed sheared flow layer, the y direction is along the sheared flow direction, and the z direction is determined by the right-hand rule, which is also along the unperturbed magnetic field direction. In this study, we only investigated the configuration with a magnetic field initially perpendicular to the sheared flow direction (i.e., $\mathbf{v}_0 \perp \mathbf{B}_0$). In this condition, the whole process is symmetric with respect to the plane $z = 0$ (Ma et al., 2017, 2021; Otto, 1999). Thus, we only need to simulate the upper-half domain, which is given by $[-L_x, L_x] \times [-L_y, L_y] \times [0, L_z]$ along the x, y, and z-directions, where $L_x = 25$, $L_y = 10$, and $L_z = 120$. The x direction is uniformly resolved by 203 grid points with the best resolution of 0.1 in the middle of the simulation domain, and the y and z directions are uniformly resolved by 203 grid points.

The initial steady state is a one-dimensional transition layer with a flow shear. The velocity profile is given by $\mathbf{v}(x) = 0.5\ \tanh(x)\mathbf{e}_y$. The density profile is given by $\rho(x) = 1/2(\rho_1 + \rho_2) + 1/2(\rho_1 - \rho_2)\ \tanh(x)$. The magnetic field B_z profile is given by $B_z(x) = 1/2(B_{z1} + B_{z2}) + 1/2(B_{z1} - B_{z2})\ \tanh(x)$. The other components of the magnetic field and velocity are set to zero. Here subscript 1 and 2 represent the value in Region 1 (i.e., $x > 0$) and Region 2 (i.e., $x < 0$), respectively. This transition layer maintains the total force balance across the sheared flow layer (i.e., the sum of the thermal pressure and magnetic pressure is constant, p_{tot}). For all simulation cases, the minimum plasma beta is always 0.5. The values of ρ_i and B_i for each case have been listed in Table 1. Whether Region 1 or Region 2 represents the magnetosheath or magnetosphere is also indicated in Table 1. Notice that for 2-D simulation, the $N = 1, 5, 10, 20, 30, 50, 100$. For Case N-M3, the density profile is proportional to the thermal pressure profile so that the temperature is constant across the sheared flow.

The KH instability is triggered by a velocity perturbation localized in the vicinity of the equatorial plane (i.e., $z = 0$), which is given by $\mathbf{v} = \nabla\Phi(x, y) \times \mathbf{e}_z f(z)$. Here, the stream function is $\Phi(x, y) = \delta v\ \cos(x/l_x)\ \cosh^{-1}(k_y y)$, $l_x = 2$, $k_y = \pi/L_y$ and $\delta v = v_y/20$, and the localization function $f(z)$ is given by $f(z) = 0.5\{\tanh[(z + z_d)/D_z] - \tanh[(z - z_d)/D_z]\}$, $z_d = 20$, and $D_z = 3$ for 3-D simulations, and $f(z) = 1$ for 2-D simulations.

The boundary conditions along the y direction are periodic. Along the x direction, the boundaries are closed, in which $v_x = 0$ and $\partial_x = 0$ for the rest of the quantities. Notice, that the dimension along x is large enough to ignore the boundary influence. To maintain the top boundary from the perturbation, an artificial friction term $-\nu(z)(\mathbf{v} - \mathbf{v_0})$ is applied to the right-hand side of the momentum equation in 3-D simulations (Ma et al., 2017). Here, $\mathbf{v_0}$ is the unperturbed bulk velocity, which also represents the solar wind or ionosphere speed. The friction term tends to force the plasma to move at its initial velocity, or equivalently it absorbs perturbations, maintaining the initial boundary layer away from the equatorial plane. Therefore, the friction coefficient is given by $\nu(z) = 0.5\{2 - \tanh[(z + z_\nu)/D_\nu] + \tanh[(z - z_\nu)/D_\nu]\}$, $z_\nu = 30$, and $D_\nu = 3$, which has been switched on only near the top and bottom boundaries (Ma et al., 2017, 2021). In this study, we applied a large dimension along the z-direction to fully damp the Alfvén wave before it reaches the top boundary during the simulation interval.

In the 3-D MHD simulation, one can always trace a magnetic field line from any given point to the top boundaries at any given time. Notice, that the top boundaries in this simulation represent the unperturbed region, the magnetic field line is considered to connect to Region 1 (2) if the location of the magnetic field line's footprint on the top boundary is in Region 1 (2). Since the whole simulation is symmetric with respect to the equatorial plane, we refer to the magnetic field line with the top on the magnetosheath (magnetospheric) side as magnetosheath

21699402, 2024, 3, Downloaded from https://agupubs.onlinelibrary.wiley.com/doi/10.1029/2023JA032234, Wiley Online Library on [17/05/2024]. See the Terms and Conditions (https://onlinelibrary.wiley.com/terms-and-conditions) on Wiley Online Library for rules of use; OA articles are governed by the applicable Creative Commons License

21699402, 2024, 3, Downloaded from https://agupubs.onlinelibrary.wiley.com/doi/10.1029/2023JA032234, Wiley Online Library on [17/05/2024]. See the Terms and Conditions (https://onlinelibrary.wiley.com/terms-and-conditions) on Wiley Online Library for rules of use; OA articles are governed by the applicable Creative Commons License

(magnetospheric) field lines. A magnetic field line with one end connecting to the magnetosheath side and the other end connecting to the magnetospheric side is referred to as an open field line. For Cases N-M1, N-M2, and N-M3, we also trace the 401×401 fluid parcels $d\mathbf{x}/dt = \mathbf{u}(\mathbf{x}(t))$ in the equatorial plane, uniformly covering area of $[-20, 20] \times [-10, 10]$ from $t = 0$, which gives a resolution of $dx = 0.1$, $dy = 0.05$. Thus, for each fluid parcel, the magnetic flux associated with this fluid parcel is given by $d\Phi = B_0 dxdy$, in which B is the magnetic field in the location of the fluid parcel at $t = 0$. For each fluid parcel, we also trace the magnetic field line that goes through this fluid parcel at each snap-shot (i.e., one Alfvén time). If the footprint of the field line on the top boundary changes from Region 1 (2) to Region 2 (1), then this field line experiences a double-reconnection process, and the total double reconnected magnetic flux is the integration of this type of magnetic flux (Ma et al., 2017, 2021).

2.2. Test Particle Simulation

The full set of non-relativistic Lorentz equations are solved using the traditional Boris method (Boris, 1970), which has been used to investigate high-energy particles in the cusp diamagnetic cavity (Nykyri et al., 2012), and KH instability (Ma et al., 2019, 2021). Linear interpolation is applied to obtain the magnetic field $\mathbf{B}$ and bulk velocity $\mathbf{u}$ at any given time, in which the magnetic field and bulk velocity are from the MHD simulations one snapshot every Alfvén time. The electric field at the ion's position is given by $\mathbf{E} = \mathbf{B} \times \mathbf{u}$ to eliminate the parallel electric field introduced by the temporal interpolation method. The velocity distribution function for any given point at any time during the simulation interval can be obtained by temporal forward tracing particles, representing the evolution of the whole 6-dimensional phase space density from the beginning of the simulation, which requires a large number of test particles. To investigate the particle velocity distributions for the selected points at any given time, it is efficient to trace the particle temporally backward and reconstruct the velocity distribution function with the assumption of Liouville's theory (Birn et al., 1997, 1998). The symmetric treatment of the time derivative in the Boris method maintains the temporal reversibility of the Lorentz equation. Thus, this code is suitable for the backward tracing method, which has been cross-validated by comparing the zero-to second-order moments of velocity distribution functions using the forward tracing and backward tracing methods in a 3-D KH instability MHD simulation (Ma et al., 2021). To find the ion phase space density $f(\mathbf{x}, \mathbf{v}, t)$ at the point $\mathbf{x}$ with a velocity $\mathbf{v}$ at time t, an ion with velocity $\mathbf{v}$ is launched from point $\mathbf{x}$ and traced backward in time to $t = 0$ when the ion was located at $\mathbf{X}$ with a velocity of $\mathbf{v}(t = 0)$. Then with the assumption that Liouville's theory is satisfied, the ion phase space density is estimated based on the shifted Maxwellian distribution, which is given by $f(\mathbf{X}, \mathbf{v}) = n(2\pi T)^{-3/2} \exp[(\mathbf{v} - \mathbf{u})^2/(2T)]$, where n, T, u is the number density, temperature, and bulk velocity in point X at $t = 0$. In this study, the velocity resolution is 0.08, and the results are convergent when using a higher velocity resolution. During the test particle simulation, the time step was chosen to fully resolve the gyro-radius motion, and the results are convergent to smaller time steps.

3. Density Asymmetry

3.1. KH Growth Rate

The linear theory Equation 1 shows that strong density asymmetry decreases the KH growth rate with an asymptotic behavior $\gamma \propto \sqrt{\rho_1/\rho_2}$, where $\rho_1 \ll \rho_2$. This is easily understandable since the flow with a small density has relatively lower energy to change the direction of the flow with heavy mass. In this study, we carried out a series of 2-D MHD KH instability simulations (i.e., Case 2D-N, $N = 1, 5, 10, 20, 30, 50, 100$), which maintains $\rho_1 + \rho_2 = 4$ and changes ρ_2/ρ_1 from 1 to 100. Figure 1a plots the growth of the KH instability (i.e., range of the normal velocity, $\Delta u_x = \max(u_x) - \min(u_x)$ as a function of time) for different density ratios. This shows that the KH instability's growth is not sensitive to the density ratio. Notice, that the Δu_x temporal profile always shows a small dip at the beginning of the simulation, indicating the system needs relaxation of a few Alfvén times, which is likely because the initial perturbation is not the exact eigenmode. For better visualization, we shift the start time to the time corresponding to the minimum of Δu_x and re-normalize the velocity so that the minimum of Δu_x is the same for all cases. Notice, that this operation will not change the growth rate of KH instability. We also estimate the KH growth rate γ by linearly fitting the $\ln(\Delta u_x)$ as a function of time in the linear stage (i.e., $0 < t < 35$), which is ≈ 0.05 for all cases. Figure 1b plots the KH growth rate as a function of density ratio from simulations (black line) and linear theory (red line). To easily compare the tendency, these two lines are normalized by their value at $\rho_2/\rho_1 = 1$, which clearly shows that the KH growth rate does not decrease as the prediction of the linear theory.

21699402, 2024, 3, Downloaded from https://agupubs.onlinelibrary.wiley.com/doi/10.1029/2023JA032234, Wiley Online Library on [17/05/2024]. See the Terms and Conditions (https://onlinelibrary.wiley.com/terms-and-conditions) on Wiley Online Library for rules of use; OA articles are governed by the applicable Creative Commons License

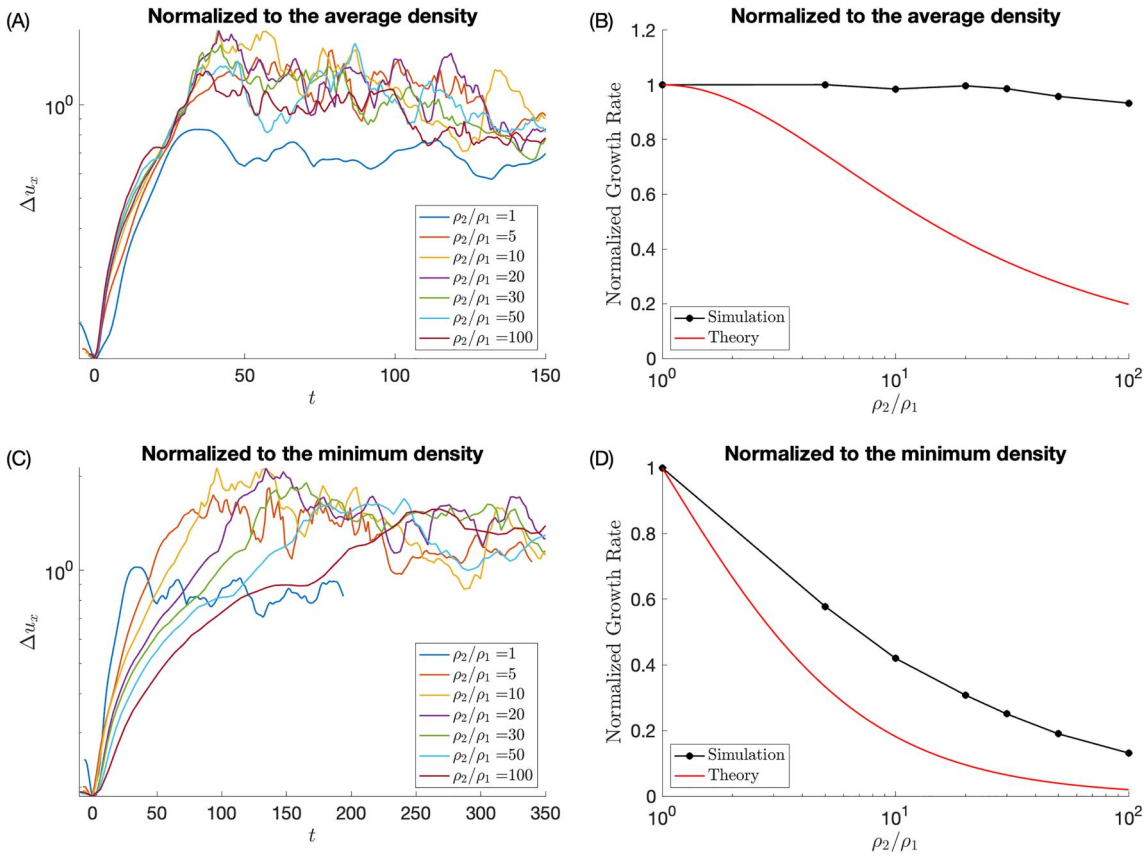

Figure 1. Panel (a) shows the range of the normal velocity Δu_x as a function of time for different density ratios, and Panel (b) shows the normalized Kelvin-Helmholtz instability growth rate as a function of density ratio (black dots) and compares with the linear theory value (red line). Panels (c) and (d) re-normalize Panels (a) and (b) based on the minimum density, respectively.

This deviation between numerical simulation and linear theory is due to the compressibility included in the numerical simulation. For the compressible fluid system, the fastest information propagation speed is the local fast mode speed (i.e., $u_f = \sqrt{u_A^2 + c_s^2}$, where u_A is the Alfvén speed and the c_s is the ion acoustic speed). Flow shear with a velocity greater than the fast mode speed prevents information of the obstacle from propagating to the upstream region, which suppresses the growth of the KH instability (Miura, 1984). Thus, the KH growth rate no longer increases with the increase of flow shear, a maximum growth rate is associated with a value between zero and the fast mode speed. For asymmetric density conditions, the fast mode speeds, and the associated Mach numbers, from both sides of the sheared flow layer, are different, which adjusts the KH instability growth rate.

One should also keep in mind, that the conclusion of comparing asymmetric configuration depends on the "reference point." For instance, Figures 1c and 1d show the results of re-normalizing the result of Figures 1a and 1b based on the minimum density, respectively. In this normalization, ρ_1 always equates to one, and ρ_2 varies from 1 to 100. As such, the growth rate decreases with the increase of ρ_2, which is consistent with what we would expect as well as the study by Amerstorfer et al. (2010). Notice, that the velocity is normalized to the Alfvén speed, which is also dependent on the density. Therefore, the re-normalization of the density also affects the value of the normalized velocity, which leads to a faster decrease in the red line in Figure 1d. However, the growth rate from numerical simulation still decreases more slowly than the linear theory prediction, which is consistent with the results based on normalization by the average density (i.e., Figure 1b).

It has been shown that the fastest mode occurs near $4\pi a/L \approx 0.5 \sim 1$, where L is the KH wavelength and a is the half-width of the flow shear (Amerstorfer et al., 2010; Miura & Pritchett, 1982), which yields $L \approx 4\pi \sim 8\pi = 12.6 \sim 25.2$, being close to our simulation domain along the y-direction (i.e., 20). Thus, the growth rate of our simulation is close to the fastest growth rate. Since the relationship between KH growth rate and the

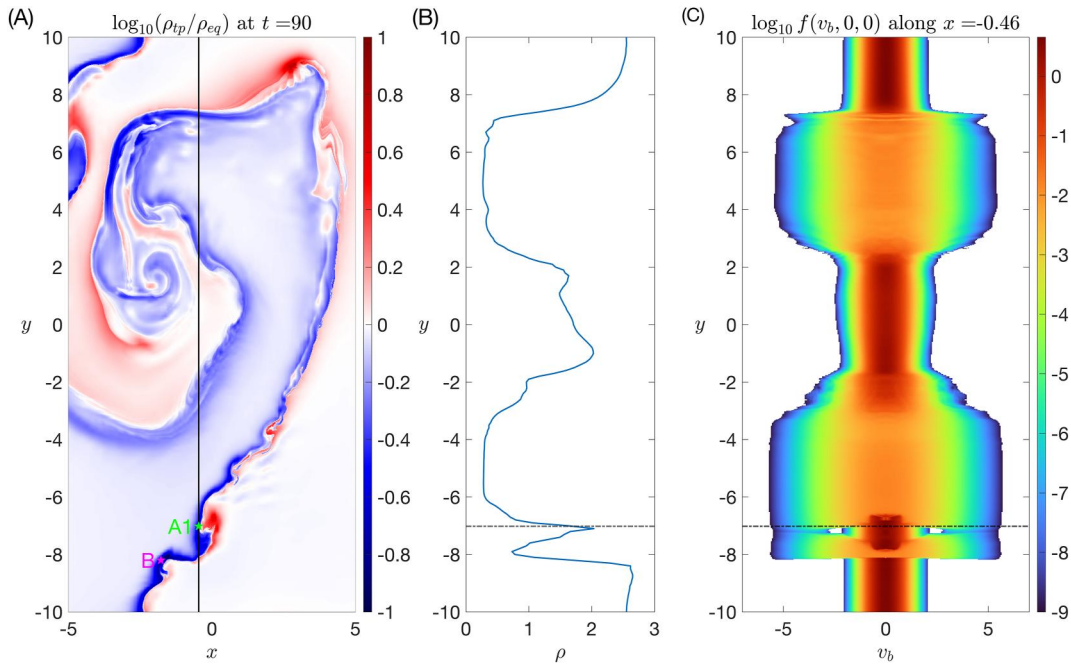

Figure 2. Panel (a) shows the ratio of the density on the equatorial plane and top boundary along the same field line. The green and magenta stars indicate the location of selected fluid parcels, Point A1 and Point B, respectively. Panels (b and c) show the density and the ion parallel velocity distribution function along the black line in Panel (a), respectively.

wavelength has been well studied by Miura and Pritchett (1982); and Amerstorfer et al. (2010). We will not study the influence of the wavelength in this study. To avoid the change in the growth rate due to different wavelengths, we fix the KH wavelength (i.e., the simulation domain along the y-direction) for all 2-D and 3-D simulations.

3.2. Particle Mixing With Different Temperatures

Under northward IMF conditions, a magnetospheric magnetic flux tube that has undergone the DMLR process driven by the 3-D KH vortex, is composed of part of a low-latitude magnetosheath flux tube and two parts of a high-latitude magnetospheric flux tube in each hemisphere, and vice versa. Thus, the density in this newly reconnected magnetospheric flux tube at low latitudes is much higher than the density in the same flux tube at high latitudes. Figure 2a plots the ratio between the density in the equatorial plane, ρ_{eq}, and density at the top boundary, ρ_{tp}, along the same field line (i.e., ρ_{tp}/ρ_{eq}) on the equatorial plane in the nonlinear stage (i.e., $t = 90$) of Case N-D, in which the dark blue region indicates the double-reconnected magnetospheric magnetic flux and the dark red region indicates the double-reconnected magnetosheath magnetic flux. Figure 2b is the density profile of the black line in Figure 2a and (ie., $x = -0.46$ in the equatorial plane), showing that this line crosses the magnetosheath region (i.e., high-density region) and magnetospheric region (i.e., low-density region) multiple times. Notice, that for case N-D, a strong density asymmetry between the magnetosphere and magnetosheath with a uniform magnetic field across the boundary indicates a strong temperature asymmetry between the magnetosphere and magnetosheath. Figure 2c is the reconstructed ion parallel velocity (i.e., v_b) distribution along the black line by using backward tracing test particle simulation with an assumption of Liouville's theorem. The narrow band with a dark red color indicates a cold dense plasma, which indicates the magnetosheath plasma. The broadband with a light red color indicates a hot tenuous plasma, being the indication of the magnetospheric plasma. The parallel velocity distribution function also shows a transition layer between the magnetosphere and magnetosheath (e.g., near $y \approx -3$), in which the maximum value decreases about one order of magnitude while the distribution becomes broad. The plasma mixing from the magnetosheath and magnetosphere can also be observed near $y = -7$, where both the dark red region and broad distribution appear simultaneously. In some points, the parallel velocity even shows a pair of small dips (i.e., the white area, being located outside of the magnetosheath ion distribution, and inside of the magnetosphere ion distribution), clearly indicating that there are three populations of the plasma present in this region. The ions with a parallel speed lower than the white areas are the cold magnetosheath

21699402, 2024, 3, Downloaded from https://agupubs.onlinelibrary.wiley.com/doi/10.1029/2023JA032234, Wiley Online Library on [17/05/2024]. See the Terms and Conditions (https://onlinelibrary.wiley.com/terms-and-conditions) on Wiley Online Library for rules of use; OA articles are governed by the applicable Creative Commons License

21699402, 2024, 3, Downloaded from https://agupubs.onlinelibrary.wiley.com/doi/10.1029/2023JA032234, Wiley Online Library on [17/05/2024]. See the Terms and Conditions (https://onlinelibrary.wiley.com/terms-and-conditions) on Wiley Online Library for rules of use; OA articles are governed by the applicable Creative Commons License

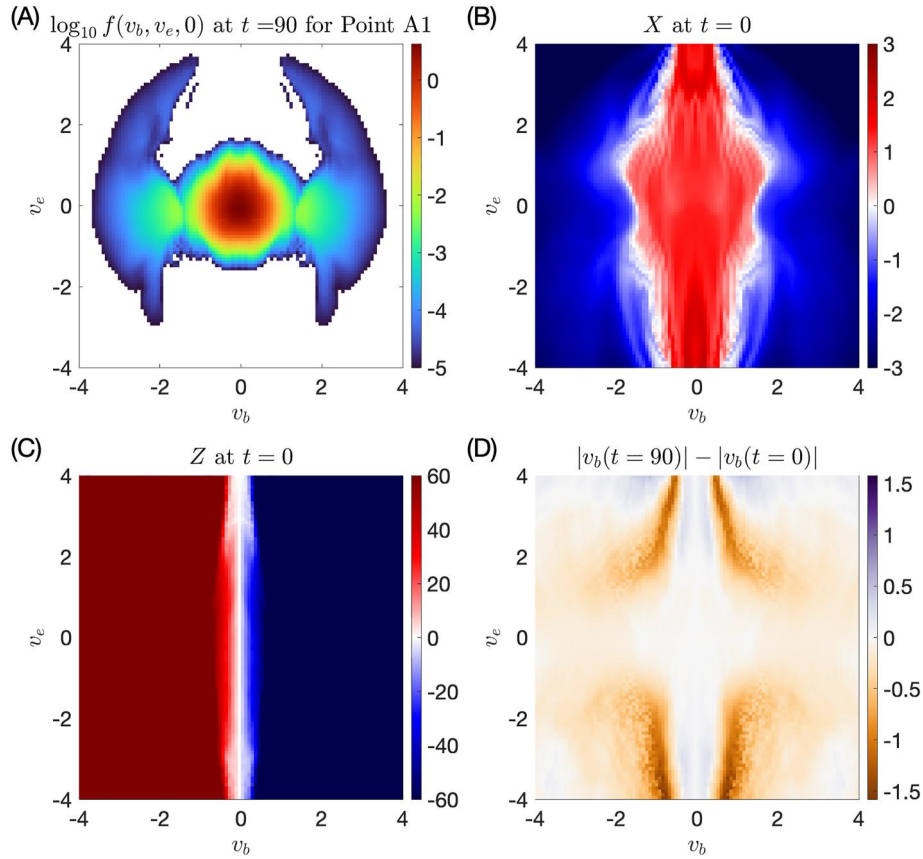

Figure 3. Panel (a) shows the velocity distribution in the phase space $v_b v_e$-plane at $t = 90$ for Point A1 in Figure 2a. Panels (b) and (c) show the X and Z components of the particles' original location for Point A1, respectively. Panel (d) shows the change of the parallel velocity magnitude for Point A1.

population, while the ions with a parallel speed higher than the white areas are the hot magnetospheric population from the high latitudes on each hemisphere, and the pair of dips indicate the magnetospheric ions with a lower parallel speed have not yet reached these points.

Figure 3a plots the velocity distribution in the phase space $v_b v_e$-plane for Point A1 on the equatorial plane at $t = 90$ (i.e., green star in Figure 2a and black dashed lines in Figures 2b and 2c), showing a cold population in the center with two distinct ion beams that propagate both parallel and anti-parallel to the local magnetic field. Here, v_e is the unit vector along the direction of $\mathbf{B} \times \mathbf{u}$. This distribution of two counter-streaming ion beams appears to be similar to the observational results during the 8 September 2015 MMS KH instability event (Eriksson, Lavraud, et al., 2016; Eriksson, Wilder, et al., 2016). Figures 3b and 3c plot the x and z coordinates of the location of the test particles at $t = 0$ (i.e., the original location of the ion), respectively, showing that the cold population is from the low-latitude magnetosheath and the two counter-streaming ion beams come from the high-latitude magnetospheric region of both hemispheres, which is consistent with the scenario of the DMLR process (Eriksson et al., 2021). Figure 3d compares the parallel velocity at $t = 0$ and at $t = 90$, indicating that these two counter-streaming beams have not been strongly accelerated. This result suggests that the formation of the counter-streaming beams can be simply due to the mixing of the plasma with different temperatures via the change of the flux tube connection, even without involving the acceleration by the reconnection parallel electric field.

Figure 4 illustrates the evolution of the magnetic field line that goes through the fluid parcel Point A1 in the xz plane in Panel (a) and a 3-D perspective in Panel (b). Here the fluid parcel trajectory is obtained through the backward tracing of Point A1 from $t = 90$ by numerically solving $d\mathbf{x}/dt = \mathbf{u}(\mathbf{x}(t))$. This selected magnetic field line has a high density and a footprint at the top boundary on the magnetosheath side at $t = 85$, which is a typical magnetosheath field line. However, this field line has a high density (i.e., $\rho > \rho_0$, here ρ_0 is the density in $x = 0$ at $t = 0$) at low latitudes (i.e., $|z| < 7$) and low density at high latitudes (i.e., $|z| > 7$) with a footprint at the top

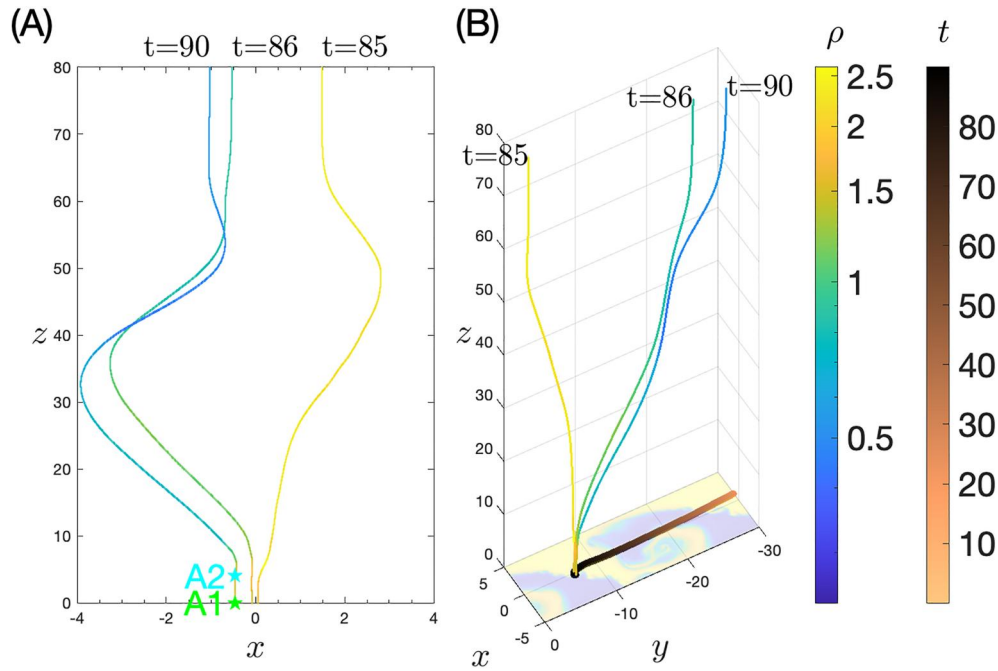

Figure 4. The evolution of the magnetic field line that goes through the fluid parcel Point (a) Panel (a) shows the magnetic field lines at $t = 85$, 86, and 90, in the xz-plane, and Panel (b) shows the same magnetic field lines in a 3-D perspective and the density in the equatorial plane. The green and cyan stars indicate the location of Points A1 and A2, respectively. The brown-to-black line in the equatorial plane is the trajectory of the fluid parcel Point (a) The blue-to-yellow color bar represents the density, while the brown-to-black color bar indicates the time.

boundary on the magnetosheath size at $t = 86$, indicating the change of flux connection due to a magnetic reconnection site near around $z = 7$. Recall, that Figure 3a shows the parallel speed of the magnetospheric population is greater than about 1.45, and reconnection occurs about $dt = 4$ earlier than the "observational time," which means the slowest magnetospheric ion travels about $dL \approx 6$ from the reconnection site to the "observation point", being close to the distance between the Point A1 and the reconnection site. Notice, that this reconnection site is very close to the equatorial plane because it is generated by the secondary KH instability, which can be observed in Figure 2a. At $t = 90$, the magnetic field line has a similar pattern as the magnetic field line at $t = 86$, however, the density at high latitude becomes lower and the footprint at the top boundary connects to the further magnetospheric direction (e.g., negative x direction), indicating that it could have experienced another reconnection process. However, this second reconnection process occurs between two magnetospheric magnetic field lines. This also gives us a hint that a clear distribution of two counter-streaming ion beams with a cold thermal population could be easier observed in a small separation of double reconnection sites since a large separation of reconnection sites requires a longer travel time from one reconnection site to the middle of the two reconnection sites. During this interval, the ongoing reconnecting process will continuously change the flux connection, which brings a different component of the ion population and further modifies the particle distribution.

One should keep in mind, that the detailed ion velocity distribution functions could be somewhat sensitive to the experience of magnetic flux and the observational location and time. Figure 5 shows two examples, which are close to Point A1 but with different ion velocity distribution functions. Figure 5a shows the ion velocity distribution in the phase space $v_b v_e$-plane for Point A2, which is along the same magnetic field line as Point A1 but away from the equatorial plane, being close to the reconnection site in the North Hemisphere. Thus, the high-latitude ions with an anti-parallel velocity in the North Hemisphere can easily reach Point A2, appearing to connect with the cold magnetosheath population. However, ions from the South Hemisphere require a relatively higher parallel speed to reach Point A2, which appears a small distinguished distribution with a low density. Figure 5b shows a ring/shell ion distribution in the phase space $v_b v_e$-plane for Point B, which is also close to the magnetosheath and magnetosphere boundary. The formation of this distribution is due to the change of flux tube connection via the DMLR process as well as finite gyroradius motion near the equatorial panel. All these different

21699402, 2024, 3, Downloaded from https://agupubs.onlinelibrary.wiley.com/doi/10.1029/2023JA032234, Wiley Online Library on [17/05/2024]. See the Terms and Conditions (https://onlinelibrary.wiley.com/terms-and-conditions) on Wiley Online Library for rules of use; OA articles are governed by the applicable Creative Commons License

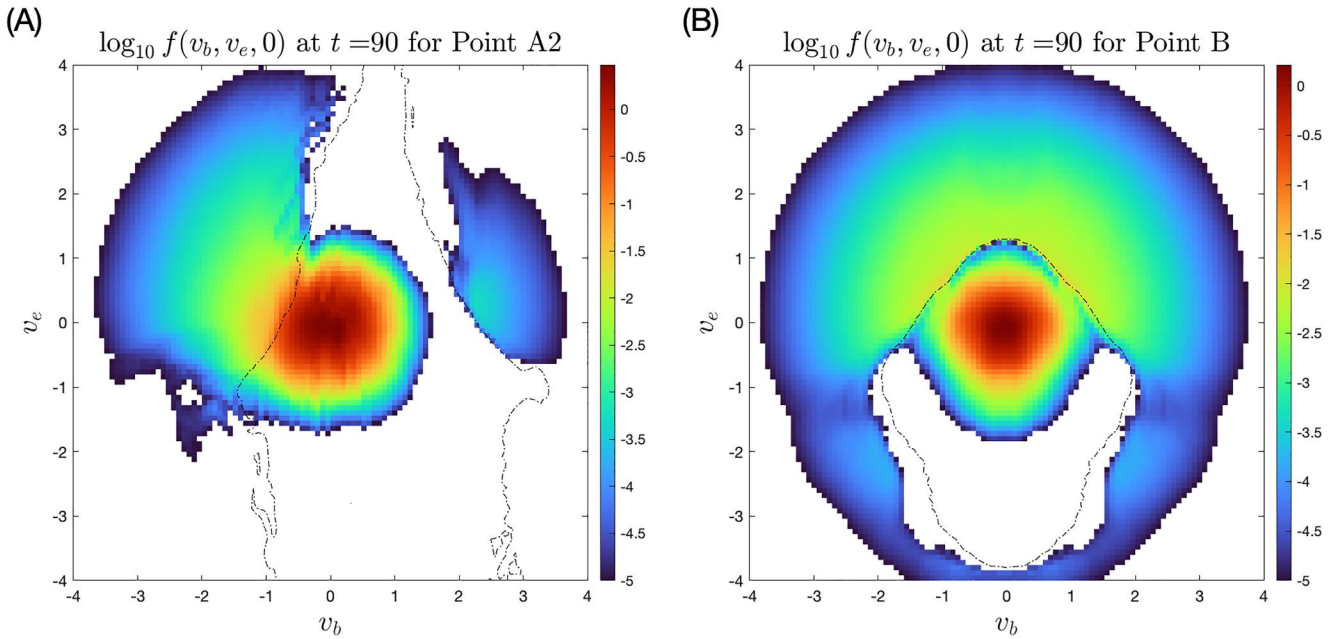

Figure 5. Panels (a and b) show the velocity distribution in the phase space $v_b v_e$-plane for Point A2 (see Figure 4a) and Point B (see Figure 2a) at $t = 90$. The dashed black contour indicates that the x coordinates of the location of the test particles at $t = 0$ equator to zero, (i.e., the separation of magnetosheath and magnetosphere population).

types of non-Maxwellian distributions indicate temperature anisotropy, which consequently can trigger different types of secondary instability. These secondary processes will eventually dissipate the free energy and form a new Maxwellian distribution.

4. Magnetic Asymmetry

4.1. Reconnected Flux

Figure 6a plots the range of the u_x as a function of time for different magnetic fields (i.e., CASE N-M1, N-M2, N-M3, S-M1, S-M2, and S-M3). For better visualization, we shift the start time to the time corresponding to the minimum of Δu_x and re-normalize the velocity so that the minimum of Δu_x is the same for all cases. Figure 6a shows that the growth rate is identical for all six cases, which is consistent with linear theory. There are several spikes in the nonlinear stage in some cases, which is due to the smaller-scale secondary instabilities (e.g., magnetic reconnection, and secondary KH instability). This panel demonstrates that the KH growth rate under southward IMF conditions is the same as the KH growth rate under northward IMF conditions if other conditions are the same. However, for southward IMF conditions, the width of the initial flow shear can be modified by the growth of magnetic reconnection. Therefore, with the interaction between the KH instability and magnetic reconnection, the observational signature of KH instability can hardly be recognized under southward IMF conditions, which does not mean that the KH instability prefers northward IMF conditions. The identical growth rates also indicate the sizes of the KH vortex in the nonlinear stage are mostly the same.

For northward IMF conditions, the DMLR process exchanges a part of the magnetosheath flux tube with a part of the magnetospheric flux tube at low latitudes. Thus, the double-reconnected magnetic flux in the magnetosphere must equate to the double-reconnected magnetic flux in the magnetosheath. This means that if the magnetospheric magnetic field is weaker than the magnetosheath magnetic field, more area on the magnetospheric side must be involved to participate in the exchange process driven by the KH instability. The red lines in Figure 6b represent the double-reconnected flux for different magnetic fields under northward IMF conditions. The symmetric case (i.e., $B_{1z} : B_{2z} = 1 : 1$) serves as the reference case, which has a total double-reconnected flux of 60. Reducing the magnetospheric magnetic field to 0.5 (i.e., $B_{1z} : B_{2z} = 1 : 0.5$) decreases the total double-reconnected flux to about 35, which is close to half of the value in the symmetric case. This indicates that the area associated with the double-reconnection process in the magnetosheath remains the same, while the area associated with the double-reconnection process in the magnetosphere reduces to about half of its value in the symmetric case. Increasing the

21699402, 2024, 3, Downloaded from https://agupubs.onlinelibrary.wiley.com/doi/10.1029/2023JA032234, Wiley Online Library on [17/05/2024]. See the Terms and Conditions (https://onlinelibrary.wiley.com/terms-and-conditions) on Wiley Online Library for rules of use; OA articles are governed by the applicable Creative Commons License

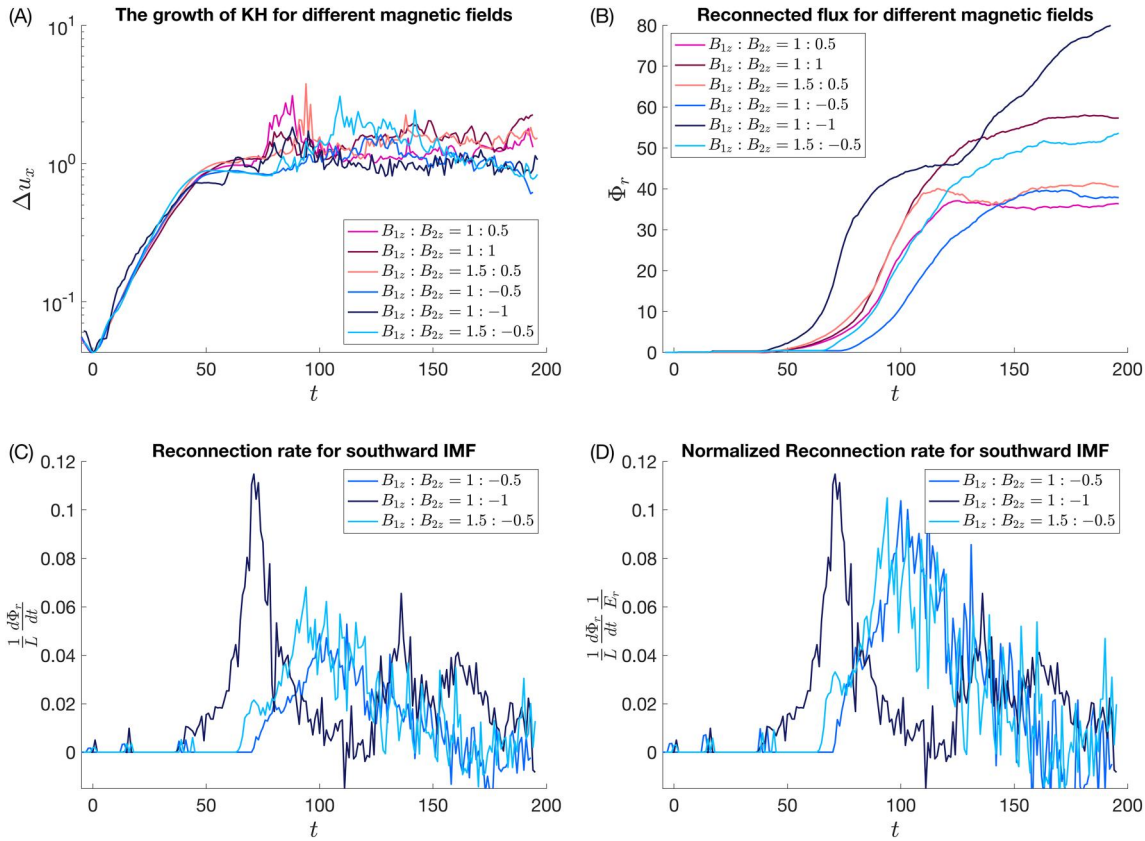

Figure 6. Panel (a) shows the range of the u_x as a function of time for different magnetic fields, and Panel (b) shows the reconnected flux for different magnetic fields. Panel (c) shows the reconnection rate for southward interplanetary magnetic field conditions, and Panel (d) re-normalizes the values in Panel (c) based on the asymmetric reconnection rate.

magnetosheath magnetic field to 1.5 (i.e., $B_{1z} : B_{2z} = 1.5 : 0.5$) does not change the total double-reconnected flux, suggesting no more area in the magnetosphere can participate in the DRLM process. Notice, that the area associated with the double-reconnection process is also proportional to the size of KH instability, being determined by the growth of the KH instability, which is identical in these three cases. Thus, one can conclude that the total double-reconnected flux is determined by the magnetic field with the weaker strength and the growth of the KH instability. Furthermore, the net transport mass through the DRLM process is only dependent on the growth of the KH instability.

For southward IMF conditions, the KH instability and magnetic reconnection can operate simultaneously. In this case, magnetic reconnection occurs at low latitudes, connecting the magnetosheath magnetic field line with the magnetospheric magnetic field, which generates a significant amount of open flux (Ma et al., 2014a, 2014b). The blue lines in Figure 6b represent the open flux, Φ_r, for different magnetic fields under southward IMF conditions, showing different case saturates at different total open flux at the end of the simulation, regardless of the identical KH growth rate for all those cases. The saturation of the open flux is because the initial current layer is widened by the KH instability as a macro-scale diffuse process (Ma et al., 2014b). However, the value of the total open flux is not simply dependent on the KH growth rate. It has been shown that the KHI can generate multiple thin layers in the nonlinear stage, these multiple thin current layers can trigger patchy reconnection (Ma et al., 2014a). In this situation, a magnetic field line can experience multiple reconnection sites, and whether it is an open or closed field line can be changed rapidly, which is the cause of strong fluctuations in reconnection rate.

Figure 6c plots the reconnected rate $(d\Phi_r/dt)/L$ for the blue lines in Figure 6b. Here, the derivative of open flux with respect to time $(d\Phi_r/dt)$, is normalized by the dimension along the y direction (i.e., $L = 2L_y$) to compare with the reconnection rate based on 2-D geometry. The symmetric case (i.e., $B_{1z} : B_{2z} = 1 : -1$) serves as the reference case, which has a maximum reconnection rate of about 0.12, being close to the Petschek reconnection rate. In this

21699402, 2024, 3, Downloaded from https://agupubs.onlinelibrary.wiley.com/doi/10.1029/2023JA032234, Wiley Online Library on [17/05/2024]. See the Terms and Conditions (https://onlinelibrary.wiley.com/terms-and-conditions) on Wiley Online Library for rules of use; OA articles are governed by the applicable Creative Commons License

21699402, 2024, 3, Downloaded from https://agupubs.onlinelibrary.wiley.com/doi/10.1029/2023JA032234, Wiley Online Library on [17/05/2024]. See the Terms and Conditions (https://onlinelibrary.wiley.com/terms-and-conditions) on Wiley Online Library for rules of use; OA articles are governed by the applicable Creative Commons License

case, reconnection is switched on at the beginning of the nonlinear stage, which is the time when the current layer is thin enough to trigger magnetic reconnection. This moment is somehow determined by the detailed dynamics of the KH instability. As a comparison, the asymmetric case with a weaker magnetosheath magnetic field but the same initial current density (i.e., $B_{1z} : B_{2z} = 1.5 : -0.5$) triggers magnetic reconnection about 20 Alfvén time later, with a lower maximum value. The other asymmetric case with a smaller initial current density (i.e., $B_{1z} : B_{2z} = 1 : -0.5$) has only a slightly later reconnection onset time and a lower reconnection rate. Theoretical studies of reconnection have demonstrated that the asymmetric reconnection rate without being influenced by the flow shear is proportional to $E_r = (B_1 B_2)^{3/2}/(B_1 + B_2)$ (Cassak & Shay, 2007). The blues lines in Figure 6d represent the reconnection rate in Figure 6c normalized by E_r, showing an almost identical maximum normalized reconnection rate for all three cases, which suggests that the scaling for typical asymmetric reconnection conditions also applies to magnetic reconnection interacting with the KH instability. This is likely because reconnection is a local process with respect to the KH instability. Although, strong flow shear exists in the system, which eventually tears the open flux along the flow direction (La Belle-Hamer et al., 1995). The reconnection electron diffusion region (EDR) is about a few electron inertial scales since the frozen-in condition is broken in the electron inertial scales. The plasma momentum is mainly carried by ions, thus the width of ion flow shear is limited by the kinetic processes on the ion inertial scale (e.g., finite gyroradius effect). Therefore, the total flow jump across the reconnection EDR region can be negligible. Thus, the scaling analysis that ignores the flow shear can still be applicable for reconnection interacting with the KH instability. This result also indicates that the fast reconnection rate during the interaction between the KH instability and magnetic reconnection is mostly due to the fast expansion of the X-line.

It is interesting to notice that magnetic reconnection starts earlier in N-M2 and N-M3 than in S-M2 and S-M3. The onset condition of magnetic reconnection is a sufficient thin current layer (or equivalently, strong anti-parallel magnetic field components). However, the mechanisms of generating anti-parallel magnetic field components by the KH instability under southward and northward are different. For northward IMF, reconnection occurs between the magnetic field B_y components, and the twist of the magnetic field generates the magnetic field B_y component through the low latitude vortex. The exact time to form a mid-latitude thin current layer likely depends on the dynamics of the KH instability and the local resistive model, which is hard to predict. For southward IMF, there is a pre-existed anti-parallel magnetic field component, which is the magnetic field B_z component. However, the KH instability can modulate the width of the current sheet and consequently control the onset time of magnetic reconnection as well as the length of the X-line. Thus, the reconnection onset time under southward and northward IMF conditions cannot be compared directly.

4.2. The Magnetic Bottle Structure in the DMLR Process

If the magnetosheath magnetic field strength is greater than the magnetospheric magnetic field, the newly reconnected magnetic field line via the DMLR process connects magnetic fields with different magnitudes, forming a magnetic bottle structure, in which the bottle body is near the equator plane for the newly reconnected magnetosheath magnetic field line, and the bottleneck is near the equator plane for the newly reconnected magnetospheric magnetic field line. Figure 7a shows the ratio of the magnetic field on the equatorial plane $B_{\rm eq}$ and top boundary $B_{\rm tp}$ along the same field line in the equatorial plane at $t = 115$ for Case N-M, in which the red and blue regions indicate the magnetic bottle body and bottleneck structures, respectively. The two brown-to-black lines are the trajectories of the selected fluid parcels, Point C and Point D. The evolution of the magnitude of the magnetic field B along the magnetic field line that goes through fluid parcels Point C and Point D are presented in Figures 7b and 7c, in which the horizontal axis represents the time, the vertical axis represents the z-coordinate of the magnetic field line, and the color index represents the magnitude of the magnetic field. These two panels show that both magnetic field lines experienced the double reconnection process at about $t = 85$ with a reconnection site at a distance of about $\Delta z = 60$ away from the equatorial plane. The ratio between the magnitude of the magnetic field in the bottle body and the bottleneck is about 1.2–1.7.

Figure 8a shows the square-like velocity distribution in the phase space $v_b v_e$-plane at $t = 115$ for Point C, being consistent with the Double Star 1 observational results (see, Figure 2f by Taylor and Lavraud (2008)). Figures 8b and 8c show the X and Z components of the particles' original location, respectively. The black lines indicate the boundary of the loss cone, based on the pitch angle $\alpha = \arcsin\sqrt{1/1.5}$ with an assumption of an average $B_{\rm max}/B_{\rm min} = 1.5$. Figure 8b shows that ions with a low parallel velocity still remain in the loss cone because there is not

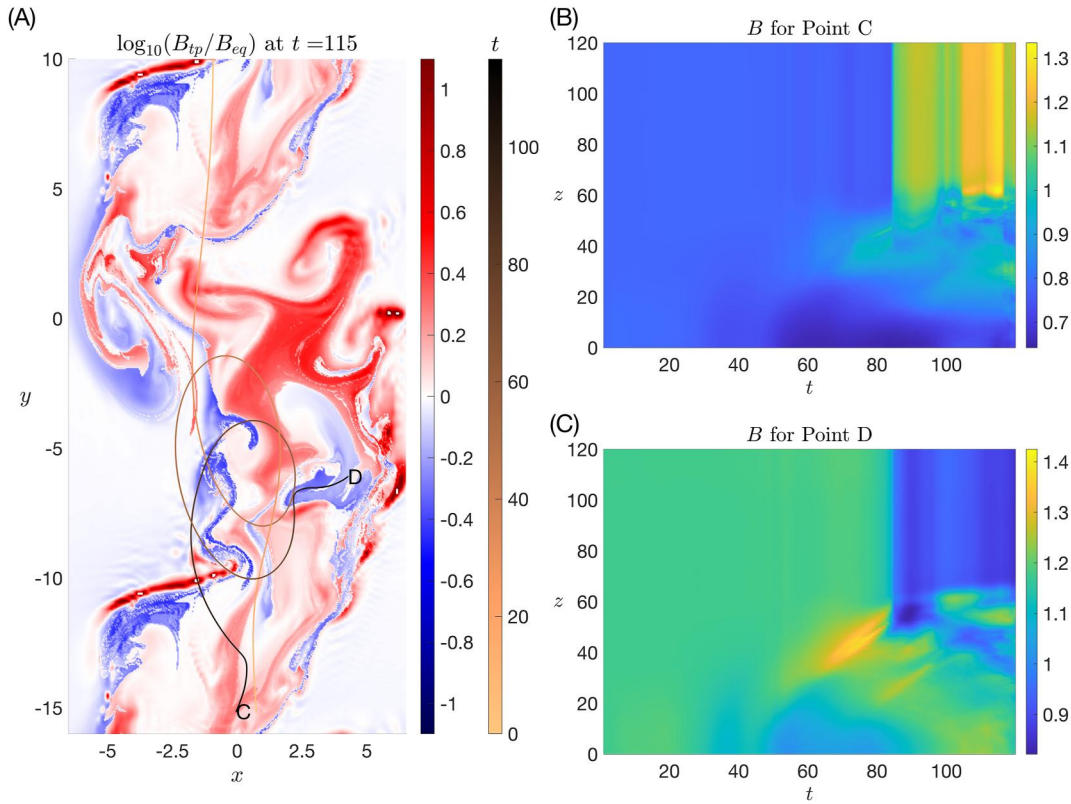

Figure 7. Panel (a) shows the ratio of the magnetic field on the equatorial plane and top boundary along the same field line at $t = 115$ for Case N-M. The brown-to-black lines in the equatorial plane are the trajectories of the selected fluid parcels, Point C and Point (d) Panels (b and c) present the evolution of magnitude of the magnetic field along the magnetic field line that goes through fluid parcels Point C and Point D, respectively.

enough time for these particles to leave the loss cone. Here, the separation between the magnetosheath and the magnetospheric population is about $v_b = 2$. Notice, that double reconnection occurred at about $t = 85$, (i.e., $\Delta t = 30$ earlier than the observational time). This yields a reconnection site about $\Delta z = v_b \Delta t = 60$ away from the observational point, being consistent with Figure 7b. Figure 8c further confirms that the trapped population mostly comes from the low-latitude regions. The trapped ions from high latitudes have high field-aligned speeds, which have been reflected by the mirror point. Notice, that the Fermi acceleration between two approaching mirror points is a common mechanism to increase the parallel speed. Figure 8d plots the change in the parallel speed, illustrating that the reflected trapped ions indeed increase the parallel speed. However, one should keep in mind, that the Fermi acceleration mechanism is not expected to be efficient for the thermal ion population in the magnetic bottle structure generated by the DMLR process via the KH instability for two reasons. First, the typical thermal ion bouncing time between the two mirror points is comparable to the KH growth time. Therefore, the thermal ions can hardly bounce multiple times before the change of the magnetic bottle structure due to the collapse of the KH vortex. In contrast, electrons or energetic ions may be accelerated more efficiently in the magnetic bottle structure. However, a detailed analysis is out of the scope of this paper, but it has been discussed by Leroy et al. (2019). Second, once the thermal ions have been trapped in the magnetic bottle, the magnetic bottle size merely decreases unless the magnetic field line experiences a secondary KH instability. Thus, the ions can hardly be further accelerated after the first reflection.

Figure 9a plots the velocity distribution in the phase space $v_b v_e$-plane at $t = 115$ for Point D, showing three ion components. Figures 9b and 9c represent the particles' original location's X and Z components, respectively. The black lines correspond to the boundary of the "loss cone" with the assumption of $B_{\max}/B_{\min} = 1.2$. Figure 9b shows the separation between the magnetosheath and the magnetospheric population is mainly along the $|v_b| = 2$, which corresponds to the lowest speed that the magnetospheric ions reach Point D, being the same as Point C. Figure 9c also indicates the existence of reflected ions in the "trapped" region. These ions are likely trapped by the

21699402, 2024, 3, Downloaded from https://agupubs.onlinelibrary.wiley.com/doi/10.1029/2023JA032234, Wiley Online Library on [17/05/2024]. See the Terms and Conditions (https://onlinelibrary.wiley.com/terms-and-conditions) on Wiley Online Library for rules of use; OA articles are governed by the applicable Creative Commons License

21699402, 2024, 3, Downloaded from https://agupubs.onlinelibrary.wiley.com/doi/10.1029/2023JA032234, Wiley Online Library on [17/05/2024]. See the Terms and Conditions (https://onlinelibrary.wiley.com/terms-and-conditions) on Wiley Online Library for rules of use; OA articles are governed by the applicable Creative Commons License

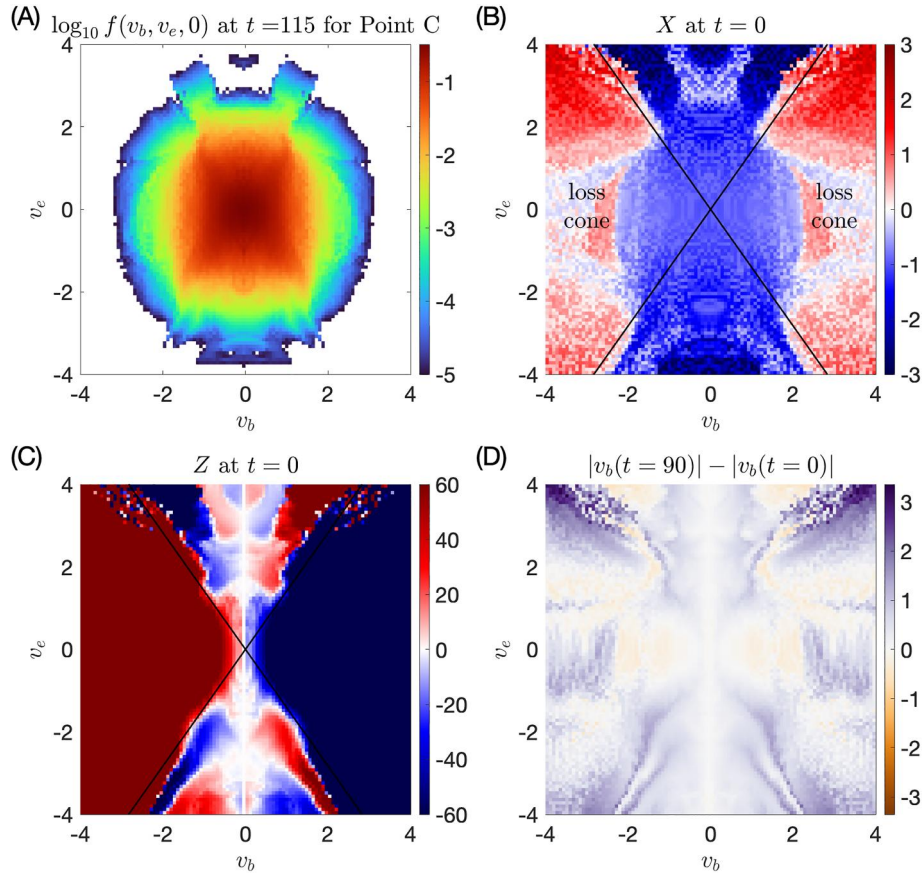

Figure 8. Panel (a) shows the velocity distribution in the phase space $v_b v_e$-plane at $t = 115$ for Point (c) Panels (b and c) show the X and Z components of the particles' original location, respectively. The black lines indicate the boundary of the loss cone. Panel (d) shows the change of the parallel velocity magnitude.

strong magnetic field near the mid-latitude, which is generated by the twisting of the magnetic field line due to the localized KH vortex before the DMLR process (see yellow region in Figure 7c). Notice, after the DMLR process, the "trapped" magnetosheath ions have no barrier to leave the low-latitude region, while the high-latitude magnetospheric ions are still trapped at the high latitudes. This structure allows the free mixing of ions in the loss cone region and dilutes the low-latitude magnetosheath population in the trapped region, forming anisotropic temperature and eventually triggering secondary instability. The net effect would help to mix the ions from both sides and increase the local specific entropy (Johnson & Wing, 2009; Johnson et al., 2014). Figure 9d shows no prominent parallel accelerating process except for the bouncing motion of the trapped ions.

5. Discussion

5.1. Transport Rate in Different Planets

Our simulation results demonstrate that the total double reconnected flux, Φ_d, is based on the KH wavelength, L, and the lower magnitude of the magnetic field, B_m, for a KH wave under the ideal case when IMF is parallel to the planet's magnetic field, which can be formally written as $\Phi_d = \alpha L^2 B_m$. Here, $\alpha < 1$ represents the width associated with the double reconnected flux (e.g., in our simulation $\alpha = 0.15$), which is determined by the growth of the KH mode. In the following estimation, we always assume that the KH mode operates at its highest growth rate, which is close to our simulation cases. Thus, we set $\alpha = 0.15$. Here, the "ideal" means that the sheared flow is perpendicular to the magnetic field in the equatorial plane, which should be considered as the upper limit of our following estimation (Ma et al., 2017). Assuming the double reconnection site is about one wavelength away from the equatorial plane (Ma et al., 2014a), the mass loss from the planet is about $M_o = 2\rho_{\mathrm{msp}} \alpha L^3$ and the loading mass

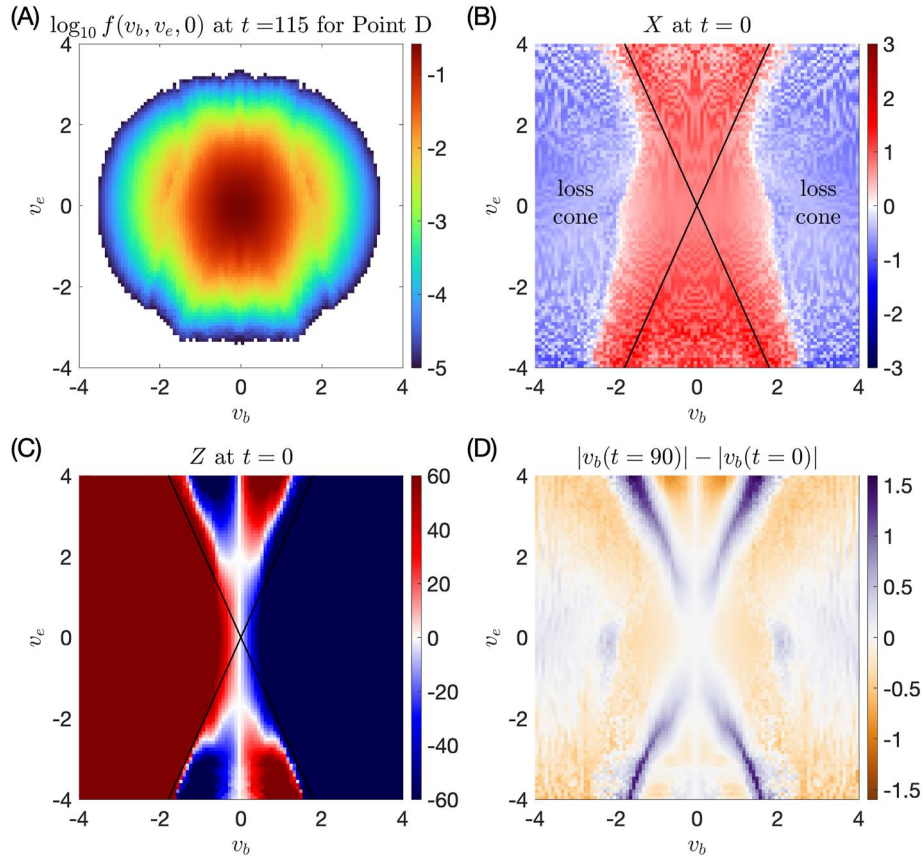

Figure 9. Panel (a) shows the velocity distribution in the phase space $v_b v_e$-plane at $t = 115$ for Point (d) Panels (b and c) show the X and Z components of the particles' original location, respectively. The black lines indicate the boundary of the loss cone. Panel (d) shows the change of the parallel velocity magnitude.

to the planet is about $M_i = 2\rho_{\mathrm{msh}}\alpha L^3$ for a KH wave. Notice, that the exchanged mass only depends on the volume being exchanged, and the density in the exchanged volume.

One can estimate the lifetime of the KH wave based on the advection time. The advection time is the duration that the KH wave moves from the subsolar point to the terminator flank region. It can be estimated by $\tau_d = L_s/u_k$, where L_s is the distance from the original of the KH instability to the place where the KH instability decays, and $u_k = (\rho_{\mathrm{msp}}u_{\mathrm{msp}} + \rho_{\mathrm{msh}}u_{\mathrm{msh}})/(\rho_{\mathrm{msp}} + \rho_{\mathrm{msh}})$ is the advection speed of the KH wave. Thus, the average double reconnection rate is Φ_d/τ_d, and the mass loading rate and loss rate are M_i/τ and M_o/τ for a single KH wave, respectively.

One can also estimate the lifetime of the KH wave based on the growth time $\tau_g = \gamma^{-1}$. Our simulation shows that the double reconnection process saturates about $3\tau_g$ after the KH wave becomes nonlinear (see Figures 1 and 6), and the duration between the linear stage to the nonlinear stage is about $\log(\Delta V/V_0)\tau_g$, where ΔV is the total velocity jump between magnetosheath and magnetosphere, and V_0 is the initial velocity perturbation, which is assumed to be 20 km s^{-1} for all planets. Thus, the time interval for KH from the initial perturbation to the saturation is about $\tau_s = [\log(\Delta V/V_0) + 3]\tau_g$.

If the KH wave is mainly moving tailward, the advection time τ_d is similar to the saturation time τ_s. However, the KH wave can also be roughly stationary due to the momentum balance between sunward co-rotational magnetospheric flow and tailward magnetosheath flow (e.g., dawnside of the giant magnetosphere) or due to the heavy ion in the magnetosphere (e.g., Venus). In this case, the KH instability can decay before it moves from the upstream region to the downstream region, where it has been observed. Therefore, the downstream KH instability is likely to be locally generated, and the whole region where KH can be observed should be considered as the KH

21699402, 2024, 3, Downloaded from https://agupubs.onlinelibrary.wiley.com/doi/10.1029/2023JA032234, Wiley Online Library on [17/05/2024]. See the Terms and Conditions (https://onlinelibrary.wiley.com/terms-and-conditions) on Wiley Online Library for rules of use; OA articles are governed by the applicable Creative Commons License

21699402, 2024, 3, Downloaded from https://agupubs.onlinelibrary.wiley.com/doi/10.1029/2023JA032234, Wiley Online Library on [17/05/2024]. See the Terms and Conditions (https://onlinelibrary.wiley.com/terms-and-conditions) on Wiley Online Library for rules of use; OA articles are governed by the applicable Creative Commons License

Table 2
Summary of the Plasma Properties for Different Planets

	Venus	Earth	Jupiter	Saturn
Solar Wind Conditions				
Velocity (km s^{-1})	300	350	378	400
Magnetic field (nT)	12	4	0.2	0.5
Cross-section length (R_P)	4	40	200	120
Magnetosheath				
Density (cm^{-3})	40	10	1	0.1
Temperature (eV)	20	100	188	200
Velocity (km s^{-1})	200	210	352	200
Magnetic field (nT)	48	16	4	5
Ion gyroradius (km)	9.5	64	350	289
Ion Inertial Length (km)	36	72	228	720
Magnetosphere/Ionosphere				
Species	O^+	H^+	O^+, S^+	H_2O^+
Density (cm^{-3})	5.9×10^3	0.5	0.01 ~ 1	0.01
Temperature (eV)	0.25	1000	188 ~ 18,800	200
Corroational speed (km s^{-1})	0	0	200	100
Magnetic field (nT)	5 ~ 20	16	4	5
Ion gyroradius (km)	2.6 ~ 10	201	350 ~ 3502	289
Ion Inertial Length (km)	12	322	911 ~ 9109	9661

active region. Thus, the average double reconnection rate is $(L_s/L)\Phi_d/\tau_s$, and the mass loading rate and loss rate are $(L_s/L)M_i/\tau_s$ and $(L_s/L)M_o/\tau_s$ for the KH active region, respectively.

The KH growth rate for each planet is estimated based on our 2-D simulation result, showing a normalized KH growth rate $\gamma_0 \approx 0.05$ in our simulation parameter. We further assume that the $\gamma \propto k\Delta V$, where $k = 2\pi/L$ is the wave-vector, and ΔV is the total velocity jump between magnetosheath and magnetosphere or ionosphere. The sum of the magnetospheric and magnetosheath number density is equal to $4n_0$. For heavy species, the number density needs to be multiplied by $\mu = m_i/m_p$, where m_i is the weight of the heavy ion. The sum of the magnetospheric and magnetosheath magnetic fields equals $2B_0$. The half-width of the initial flow shear a equates to the length scale $L0 = 3L_d$, where L_d is the maximum value of the ion gyroradius and ion inertial length on the magnetosheath side and magnetospheric or ionospheric side.

The typical values of the upstream solar wind, magnetosheath, and magnetosphere or ionosphere parameters for Venus, Earth, Jupiter, and Saturn have been listed in Table 2, the detailed reference sources for these values are discussed in the appendix. The KH properties and associated transport quantities for each planet are listed in Table 3. The program for calculating these values is available in our data package (Ma, 2023), which allows readers to validate and compare with other planets, as well as improve the estimation based on the new data.

Table 3 shows that the Earth and Juptier's KH wavelength is relatively longer compared to the local kinetic scale, while Venus and Saturn have a relatively shorter KH wavelength, which is likely due to the heavy ion species. For Earth, the advection time is comparable to the saturation time, which is consistent with our assumption. For Venus, the advection time is much longer than the saturation time due to the dense ionosphere, suggesting the KH

Table 3
Summary of the Kelvin-Helmholtz Instability Properties and Associated Transport Quantities for Different Planets

			Jupiter			Saturn		
	Venus	Earth	Dawn	Dusk	All	Dawn	Dusk	All
Wavelength (R_p)	0.4	10		20			10	
$2ka$	0.54	0.19		0.25			0.62	
Advection Distance (R_p)	1	50		132			50	
Advection Speed (km s^{-1})	0.08	200	168 ~ 276	209 ~ 331		7	136	
Advection Time (h)	22	0.44†	9 ~ 15	8 ~ 13†		113	6†	
saturation time (h)	0.02†	0.45	4.4†	13		3†	7.4	
Reconnected Flux (MWb)	0.09	19	7740	1170	8910	1272	254	1526
Reconnection Potential (kV)	1.3	12	484	27 ~ 42	510 ~ 526	115	12	127
Solar Wind Potential (kV)	87	357		1057			1398	
Particle Loading Rate ($\log_{10}s^{-1}$)	25	27	30	28	30	27	26	27
Mass Loading Rate (kg s^{-1})	0.02	1.6	566	31 ~ 49	597 ~ 615	4.5	0.5	5
Particle loss rate ($\log_{10}s^{-1}$)	27	26	28 ~ 30	27 ~ 28	28 ~ 30	26	25	26
Mass loss rate (kg s^{-1})	50	0.08	91 ~ 9050	8 ~ 497	98 ~ 9550	8	0.8	8.8
Internal Loading Rate (kg s^{-1})	0	0		260 ~ 1400			12 ~ 250	

Note. † indicate which lifetime of the Kelvin-Helmholtz wave is used to calculate the transport rate.

21699402, 2024, 3, Downloaded from https://agupubs.onlinelibrary.wiley.com/doi/10.1029/2023JA032234, Wiley Online Library on [17/05/2024]. See the Terms and Conditions (https://onlinelibrary.wiley.com/terms-and-conditions) on Wiley Online Library for rules of use; OA articles are governed by the applicable Creative Commons License

vortex is mostly stationary. For the giant magnetospheres, the advection times are much longer than the saturation times on the dawn sides and are comparable to the saturation times on the dusk sides.

For Earth, the double-reconnection potential is about 12 kV, which is close to the upper limit of viscous contribution to the convection pattern estimated by Milan (2004). As a comparison, we also calculate the solar wind potential $U = B_s u_s L_c$, where B_s is the solar wind magnetic field, u_s is the solar wind speed, and L_c is the length of the cross-section at the terminator flank region. For Earth and Venus, the double-reconnection rate is less than 5% of solar wind potential, while it is close to 50% of the solar wind potential in Jupiter, indicating the viscous-like interaction plays an important role in the solar-wind-magnetosphere coupling in Jupiter. For Saturn, the double-reconnection potential is about 10% of the solar wind potential, indicating that Saturn is an intermediate state between the Earth and Jupiter.

The plasma loading rate in the Earth is about $1 \times 10^{27} s^{-1}$, being consistent with the previous estimation (Ma et al., 2017). Table 3 confirms that the KH instability is a major ion escaping mechanism for Venus. Nevertheless, we also notice that the estimation of the loss rate for Venus is higher than the other studies (e.g., Lammer et al. (2006); Dang et al. (2022)), which could be due to the overestimation of the ionospheric density. A lower ionospheric density due to a higher boundary between the ionosphere and magnetosheath can largely reduce the loss rate by one to two orders of magnitude. One should keep in mind, that this estimation is based on the assumption that the magnetic field is not fully vanishing in the ionosphere. If the magnetic field drops at a relatively higher altitude, then the oxygen-loss rate will decrease. Both giant magnetospheres mainly lose their heavy ions on the dawn side, where the flow shear is large. The plasma loss rate for Saturn is comparable to its internal plasma source, indicating that the vicious-like interaction may be as important as the Vasyliunas (1984) cycle for Saturn's magnetospheric dynamic. Although typically the plasma loss rate for Jupiter is much smaller than its internal source, it is roughly proportional to the magnetospheric density. Thus, for a dense magnetospheric boundary due to the radial outward transport process driven by the internal interchange instability (Schok et al., 2023), the plasma loss rate can be even higher than the internal loading rate.

5.2. Expansion of X-Line

Our simulations show that the KH instability can lead to a high reconnection rate when IMF is anti-parallel to the planet's magnetic field. However, the peak reconnection rate is proportional to $E_r = (B_1 B_2)^{3/2}/(B_1 + B_2)$ (Cassak & Shay, 2007), indicating that the high reconnection rate is mainly achieved by fast expansion of the X-line. This is because reconnection is a local process with respect to the KH instability. On the length scale of the magnetic reconnection site, the flow shear is negligible. Notice, that a current sheet with a strong asymmetric magnetic field is also equivalent to a large plasma beta gradient, which can suppress the magnetic reconnection rate due to the kinetic effect (Swisdak et al., 2003). This effect cannot be simulated by using the MHD model. However, based on our analysis, it is presumable that such an effect should still apply to magnetic reconnection modified by the nonlinear KH instability. Nevertheless, this hypothesis should be validated by using hybrid or full kinetic simulations in the future.

The X-line expansion speed is important to understand the solar-wind-magnetosphere coupling from a global perspective, see detailed discussion by Walsh et al. (2018) and Zou et al. (2018, 2019). The local MHD simulations suggested that the X-line expansion speed can be highly modified by the growth of the KH instability under southward IMF conditions. Thus, measuring the X-line expansion speed from the ground observation may require a high spatial resolution of several hundred kilometers mapped to the equatorial magnetopause and a high temporal resolution of a few seconds. Meanwhile, in-situ measurement of the X-line expansion speed requires two separate groups of measurement to provide the displacement (i.e., about a few hundred kilometers) and delay time. To further separate the temporal variation from the spatial variation, each group of measurements requires at least a 2-point measurement with a separation of tens of kilometers. This type of satellite separation is not designed by any of the current missions, thus a white paper has been proposed to provide the possibility for such a measurement (Hwang et al., 2023).

It is also important to notice that both magnetic reconnection and KH instability are important mechanisms for the generation of field-aligned currents (FACs) (Ma & Otto, 2013; Johnson & Wing, 2015; Johnson et al., 2021; Wing & Johnson, 2015), which eventually affects the auroral signature. However, a quantitative

21699402, 2024, 3, Downloaded from https://agupubs.onlinelibrary.wiley.com/doi/10.1029/2023JA032234, Wiley Online Library on [17/05/2024]. See the Terms and Conditions (https://onlinelibrary.wiley.com/terms-and-conditions) on Wiley Online Library for rules of use; OA articles are governed by the applicable Creative Commons License

understanding of how the nonlinear interaction between the KH instability and reconnection affects the FACs is still an open question.

5.3. Particle Distributions

In this study, we use MHD with test particle simulations to demonstrate that two counter-streaming ion beams, ring/shell ion velocity distribution, and square-like velocity distribution, that have been observed in the KH event, can be generated by mixing the plasma through the DMLR process. In our study, we did not find a significant parallel ion acceleration process for two reasons. First, the test particle simulation does not include the parallel electric field from the MHD simulation, since the size of the parallel electric field is exaggerated by the MHD simulation. Second, the thermal ion species cannot be efficiently accelerated through the Fermi acceleration mechanism, since the bouncing time between two magnetic mirror points is comparable to the KH growth/advection speed. Thus, by the time the satellite can clearly identify the KH structure (i.e., before the KH vortex becomes turbulent), thermal ions may only have bounced one or two times between the magnetic mirror points. Furthermore, the overall size of the magnetic bottle structure generated by the DMLR process does not reduce significantly during the growth of the KH instability, which consequently, cannot provide energy to accelerate the thermal ions in the parallel direction. Nevertheless, the presence of secondary processes (e.g., KH instability and Rayleigh-Taylor instability (Matsumoto & Hoshino, 2004, 2006; Matsumoto & Seki, 2010; Yan et al., 2022, 2023)) can generate a smaller magnetic bottle structure which provides a second acceleration process and allows more bounce times between the mirror points.

This study does not include the dynamics of the electrons during the KH instability, since the electrons are more sensitive to the parallel electric field, which is more suitable to be investigated by using hybrid or full kinetic simulations. For instance, Delamere et al. (2021) show that bidirectional electron beams can be expected from the parallel electric fields associated with the strong guide field reconnection during the KH instability. Nevertheless, the electrons have smaller gyro-radii compared to the ions, thus the mechanisms for velocity distribution generated by the change of the flux connection should still be applicable to the electrons if the majority of the population does not go through the mid-latitude diffusion region. It is worth noticing that, the KH vortex bends the magnetosheath magnetic field sunward and the magnetospheric magnetic field tailward, which generates a northward and a southward current on the dawn side of the north hemisphere and south hemisphere, respectively. With a northward background magnetic field, this indicates that the DMLR process has a pole-ward parallel electric field on the dawn side, and an equator-ward parallel electric field on the dusk side. This dawn-dusk asymmetry may affect the electron dynamics during the KH instability, which should be further examined by using hybrid or full kinetic simulations.

One should also keep in mind that the mixed ion velocity distribution strongly depends on the initial magnetosheath and magnetosphere ion velocity distributions, which could be anisotropic. Such distribution could trigger kinetic instabilities, and those kinetic instabilities can be the trigger of the KH instability as well as interact with the KH instability. The detailed process is interesting but is out of the scope of this paper.

6. Summary

Strong density asymmetry and magnetic field asymmetry across sheared flow boundaries are often present at a planetary magnetopause. Our MHD simulations demonstrate that.

- The KH growth rate in the compressible system is not sensitive to the density asymmetry, which is different from the prediction by the incompressible linear theory. When IMF is parallel to the planet's magnetic field, the nonlinear KH instability can generate DMLR.
- The total double-reconnected flux depends on the lower magnitude of the magnetic field for a KH wave under the ideal case.
- Plasma with different temperature mixing via the DMLR process can form two counter-streaming ion beams as well as a ring/shell ion velocity distribution, which have been observed to generate kinetic magnetosonic waves (Eriksson et al., 2021; Moore et al., 2016, 2017).
- The asymmetric magnetic field across the sheared flow can generate the magnetic bottle structure through the DMLR process driven by the KH instability, in which both the bottle body and the bottleneck part can exist in the vicinity of the equatorial plane. The ongoing particle-loss processes outside of the loss cone

21699402, 2024, 3, Downloaded from https://agupubs.onlinelibrary.wiley.com/doi/10.1029/2023JA032234, Wiley Online Library on [17/05/2024]. See the Terms and Conditions (https://onlinelibrary.wiley.com/terms-and-conditions) on Wiley Online Library for rules of use; OA articles are governed by the applicable Creative Commons License

mixing with the plasma from the newly reconnected flux tube can form a square-like velocity distribution.

- When the IMF is anti-parallel to the planet's magnetic field, the nonlinear interaction between magnetic reconnection and the KH instability leads to a fast reconnection (i.e., close to the Petschek reconnection even without including kinetic physics). The peak value of the reconnection rate still follows the scaling of the reconnection rate without including the flow shear, because the size of the reconnection site is much smaller compared to the width of the sheared flow even during the onset of the KH instability. The fast reconnection rate is mostly due to the fast expansion of the X-line, which is increased by the growth of the KH instability.
- We also compared mass transport rate and double reconnection potential driven by the KH instability for Earth, Saturn, Jupiter, and Venus, showing that KH instability plays an important role in solar-wind-magnetosphere/ionosphere coupling in these four planets.

Appendix A: The Reference Sources for Table 2

For Earth, the typical solar wind has a density of about 4 cm^{-3} and speed of u_s = 350 km s^{-1} with an IMF B_s = 4 nT near 1 AU (Ma et al., 2020). The typical magnetosheath has a density of about 10 cm^{-3} and a temperature of about 100 eV (Ma et al., 2020) and an average bulk velocity close to $0.6u_s$ (Dimmock & Nykyri, 2013) with a magnetic field strength of about 16 nT (Dimmock & Nykyri, 2013). The magnetopause has a density of about 0.5 cm^{-3} and a temperature of about 1 keV (Ma et al., 2020) with no bulk velocity, and the magnetic field strength is close to the magnetosheath magnetic field. It has been shown that the KH wavelength can reach about 10 Earth Radii (i.e., R_E = 6371 km), at $50R_E$ away from the subsolar point (Lin et al., 2014).

For Jupiter, the typical solar wind speed is about 378 km s^{-1} (Thomsen et al., 2019) and the magnetic field is about 0.2 nT near 5.2 AU (B. Zhang et al., 2018; Nichols et al., 2017). The magnetosheath has a proton number density of about 1 cm^{-3} and a temperature of about 188 eV (Ranquist et al., 2019), and the magnetosphere has a heavy ion (e.g., O^+ and S^+) number density of about 0.01 cm^{-3} (Delamere et al., 2011). The magnetosheath bulk velocity is about 352 km s^{-1} (Ranquist et al., 2019) tailward, and magnetopause sub-co-rotational flow speed is about 200 km s^{-1} (Delamere et al., 2011). Both magnetosheath and magnetosphere are assumed to have a magnetic field of about 4 nT, and the magnetospheric temperature is assumed based on the pressure balance. The Jupiter's magnetopause standoff distance is about 63 Jupiter's Radii (i.e., R_J = 71,492 km) for the compressed state and $92R_J$ for the expanded states (Joy, 2002). Recently, the KH instability has been observed $40R_J$ tailward away from the terminator flank region by Juno satellite (Montgomery et al., 2023). The KH wavelength is assumed to be about $20R_J$ based on the MHD simulation (Zhang et al., 2018). Nevertheless, Schok et al. (2023) demonstrated that the magnetopause density can be largely modified by the radial outward transport process driven by the internal interchange instability, and the number density can reach 1 cm^{-3}.

For Saturn, the solar wind velocity is about 400 km s^{-1} (Thomsen et al., 2019) and the magnetic field is about 0.5 nT (Jia et al., 2012) near 9.5 AU. The magnetosheath has a proton number density of about 0.1 cm^{-3} and the magnetopause has a water group (i.e., H_2O^+) number density of about 0.01 cm^{-3} (Masters et al., 2010). The ion temperature is about 200 eV on both magnetospheric and magnetosheath side (Thomsen et al., 2010, 2019). The magnetosheath bulk velocity is about 200 km s^{-1} (Burkholder et al., 2017) tailward, and magnetopause sub-co-rotational flow speed is about 100 km s^{-1}. This yields a KH advection speed of 7 km s^{-1} on the dawn side and 136 km s^{-1} on the dusk side. The magnetosheath and magnetopause magnetic fields are about 5 nT. The Saturn's magnetopause standoff distance is about 20 Saturn's Radii (i.e., R_S = 60,268 km) (Kanani et al., 2010). Cassini observed that the KH instability exists $30R_S$ tailward away from the terminator flank region. It is estimated that the longest KH wavelength is about $10R_S$ (Masters et al., 2012).

For Venus, the solar wind has a density of about 10 cm^{-3}, and the IMF is about 12 nT (Dang et al., 2022; Russell et al., 2006). The solar wind speed near 0.7 AU is often estimated as about 400 km s^{-1} (e.g., Dang et al. (2022)), which is likely based on the report of solar wind speed of 440 km s^{-1} by Russell et al. (2006). However, this value could be overestimated due to the sampling during the solar maximum. Here, we estimate the typical solar wind speed near Venus is about 300 km s^{-1} based on the statistical solar wind speed at 1 AU (Ma et al., 2020). As an unmagnetized planet, the KH instability is expected to occur at the Venus ionopause. The altitude of the ionopause varies from 400 km near the subsolar point to 900 km at 90 solar zenith angle (SZA) (T. Zhang et al., 2008). Global simulations suggested that the KH wavelength L is about 2000–3000 km

21699402, 2024, 3, Downloaded from https://agupubs.onlinelibrary.wiley.com/doi/10.1029/2023JA032234, Wiley Online Library on [17/05/2024]. See the Terms and Conditions (https://onlinelibrary.wiley.com/terms-and-conditions) on Wiley Online Library for rules of use; OA articles are governed by the applicable Creative Commons License

after the terminator flank region with a travel distance of about two Venus Radii (i.e., R_V = 6051.8 km) (Dang et al., 2022; Terada et al., 2002). Notice, that for $\alpha = 0.15$, the width of the KH mode should at least be wider than αL (i.e., 300–450 km near 90 SZA), which is allowable. Assuming the oxygen number density profile near the terminator flank region is close to its value near 65 SZA, then the ionopause has an oxygen number density of 7×10^3 cm^{-3} with a temperature about 2.9×10^3 K at about 900 km altitude (Miller et al., 1984). The ionopause magnetic field varies from about 5 to 20 nT (Zhang et al., 2008). Thus, the oxygen gyroradius (≈6–11 km) and the oxygen inertial length (≈6 km) are much smaller than the KH wavelength. Assuming the magnetosheath properties basically follow the maximum compression rate of 4, the magnetosheath has a proton density of about 40 cm^{-3}, and a magnetic field about 48 nT. We further assume the average magnetopause speed is about 200 km s^{-1} (i.e., about 60 % of the solar wind speed).

The length of the cross-section at the terminator flank region for each planet is estimated based on their magnetopause model (Dang et al., 2022; Joy, 2002; Kanani et al., 2010).

Data Availability Statement

The data and visualization tools for all figures presented in this paper are publicly available (Ma, 2024). Some of the colormaps used in this study are supported by Liu (2023).

Acknowledgments
This study is supported by NASA Grants 80NSSC18K1108, 80NSSC18K1381, 80NSSC20K1279, 80NSSC22K0304, and 80NSSC23K0899, NSF Grants 2308853 and DOE DE-SC0022952. B.B. thanks for the support of NASA Grant 80NSSC22K0949.

References

Amerstorfer, U. V., Erkaev, N. V., Taubenschuss, U., & Biernat, H. K. (2010). Influence of a density increase on the evolution of the Kelvin-Helmholtz instability and vortices. *Physics of Plasmas*, *17*(7), 072901. https://doi.org/10.1063/1.3453705

Axford, W. I. (1964). Viscous interaction between the solar wind and the Earth's magnetosphere. *Planetary and Space Science*, *12*(1), 45–53. https://doi.org/10.1016/0032-0633(64)90067-4

Axford, W. I., & Hines, C. O. (1961). A unifying theory of high-latitude geophysical phenomena and geomagnetic storms. *Canadian Journal of Physics*, *39*(10), 1433–1464. https://doi.org/10.1139/p61-172

Birn, J., Thomsen, M. F., Borovsky, J. E., Reeves, G. D., McComas, D. J., Belian, R. D., & Hesse, M. (1997). Substorm ion injections: Geosynchronous observations and test particle orbits in three-dimensional dynamic MHD fields. *Journal of Geophysical Research*, *102*(A2), 2325–2341. https://doi.org/10.1029/96JA03032

Birn, J., Thomsen, M. F., Borovsky, J. E., Reeves, G. D., McComas, D. J., Belian, R. D., & Hesse, M. (1998). Substorm electron injections: Geosynchronous observations and test particle simulations. *Journal of Geophysical Research*, *103*(A5), 9235–9248. https://doi.org/10.1029/97JA02635

Blasl, K. A., Nakamura, T. K. M., Plaschke, F., Nakamura, R., Hasegawa, H., Stawarz, J. E., et al. (2022). Multi-scale observations of the magnetopause Kelvin–Helmholtz waves during southward IMF. *Physics of Plasmas*, *29*(1), 012105. https://doi.org/10.1063/5.0067370

Boris, J. (1970). *The acceleration calculation from a scalar potential*. Princeton University Plasma Physics Laboratory. Retrieved from https://books.google.com/books?id=4mzOZwEACAAJ

Burkholder, B., Delamere, P., Ma, X., Thomsen, M., Wilson, R., & Bagenal, F. (2017). Local time asymmetry of Saturn's magnetosheath flows. *Geophysical Research Letters*, *44*(12), 5877–5883. https://doi.org/10.1002/2017gl073031

Burkholder, B. L., Nykyri, K., Ma, X., Rice, R., Fuselier, S. A., Trattner, K. J., et al. (2020). Magnetospheric multiscale observation of an electron diffusion region at high latitudes. *Geophysical Research Letters*, *47*(15). https://doi.org/10.1029/2020GL087268

Cassak, P. A., & Shay, M. A. (2007). Scaling of asymmetric magnetic reconnection: General theory and collisional simulations. *Physics of Plasmas*, *14*(10), 102114. https://doi.org/10.1063/1.2795630

Chandrasekhar, S. (1961). *Hydrodynamic and hydromagnetic stability*. Dover Publications. Retrieved from http://books.google.com/books?id=oU_-6ikmidoC

Dang, T., Lei, J., Zhang, B., Zhang, T., Yao, Z., Lyon, J., et al. (2022). Oxygen ion escape at Venus associated with three-dimensional kelvin-helmholtz instability. *Geophysical Research Letters*, *49*(6). https://doi.org/10.1029/2021GL096961

Delamere, P. A., Barnes, N. P., Ma, X., & Johnson, J. R. (2021). The Kelvin-Helmholtz instability from the perspective of hybrid simulations. *Frontiers in Astronomy and Space Sciences*, *8*, 801824. https://doi.org/10.3389/fspas.2021.801824

Delamere, P. A., Wilson, R. J., Eriksson, S., & Bagenal, F. (2013). Magnetic signatures of Kelvin-Helmholtz vortices on Saturn's magnetopause: Global survey. *Journal of Geophysical Research (Space Physics)*, *118*(1), 393–404. https://doi.org/10.1029/2012JA018197

Delamere, P. A., Wilson, R. J., & Masters, A. (2011). Kelvin-Helmholtz instability at Saturn's magnetopause: Hybrid simulations. *Journal of Geophysical Research*, *116*(A10). https://doi.org/10.1029/2011JA016724

Desroche, M., Bagenal, F., Delamere, P. A., & Erkaev, N. (2012). Conditions at the expanded Jovian magnetopause and implications for the solar wind interaction. *Journal of Geophysical Research (Space Physics)*, *117*(A7), 7202. https://doi.org/10.1029/2012JA017621

Desroche, M., Bagenal, F., Delamere, P. A., & Erkaev, N. (2013). Conditions at the magnetopause of Saturn and implications for the solar wind interaction. *Journal of Geophysical Research: Space Physics*, *118*(6), 3087–3095. https://doi.org/10.1002/jgra.50294

Dimmock, A. P., & Nykyri, K. (2013). The statistical mapping of magnetosheath plasma properties based on THEMIS measurements in the magnetosheath interplanetary medium reference frame. *Journal of Geophysical Research: Space Physics*, *118*(8), 4963–4976. https://doi.org/10.1002/jgra.50465

Eriksson, S., Lavraud, B., Wilder, F. D., Stawarz, J. E., Giles, B. L., Burch, J. L., et al. (2016). Magnetospheric Multiscale observations of magnetic reconnection associated with Kelvin-Helmholtz waves. *Geophysical Research Letters*, *43*(11), 5606–5615. https://doi.org/10.1002/2016GL068783

Eriksson, S., Ma, X., Burch, J. L., Otto, A., Elkington, S., & Delamere, P. A. (2021). MMS observations of double mid-latitude reconnection ion beams in the early non-linear phase of the Kelvin-Helmholtz instability. *Frontiers in Astronomy and Space Sciences*, *8*, 760885. https://doi.org/10.3389/fspas.2021.760885

Eriksson, S., Wilder, F. D., Ergun, R. E., Schwartz, S. J., Cassak, P. A., Burch, J. L., et al. (2016). Magnetospheric multiscale observations of the electron diffusion region of large guide field magnetic reconnection. *Physical Review Letters*, *117*(1), 015001. https://doi.org/10.1103/PhysRevLett.117.015001

Faganello, M., Califano, F., Pegoraro, F., Andreussi, T., & Benkadda, S. (2012). Magnetic reconnection and Kelvin–Helmholtz instabilities at the Earths magnetopause. *Plasma Physics and Controlled Fusion*, *54*(12), 124037. https://doi.org/10.1088/0741-3335/54/12/124037

Foullon, C., Verwichte, E., Nakariakov, V. M., Nykyri, K., & Farrugia, C. J. (2011). Magnetic Kelvin-Helmholtz instability at the sun. *Apjl*, *729*(1), L8. https://doi.org/10.1088/2041-8205/729/1/L8

Foullon, C., Verwichte, E., Nykyri, K., Aschwanden, M. J., & Hannah, I. G. (2013). Kelvin-Helmholtz instability of the CME reconnection outflow layer in the low corona. *The Astrophysical Journal*, *767*(2), 170. https://doi.org/10.1088/0004-637X/767/2/170

Henry, Z. W., Nykyri, K., Moore, T. W., Dimmock, A. P., & Ma, X. (2017). On the dawn-dusk asymmetry of the Kelvin-Helmholtz instability between 2007 and 2013. *Journal of Geophysical Research: Space Physics*, *122*(12), 11888–11900. https://doi.org/10.1002/2017JA024548

Hwang, K.-J., Goldstein, M. L., Kuznetsova, M. M., Wang, Y., ViñAs, A. F., & Sibeck, D. G. (2012). The first in situ observation of Kelvin-Helmholtz waves at high-latitude magnetopause during strongly dawnward interplanetary magnetic field conditions. *Journal of Geophysical Research: Space Physics)*, *117*(A8), 8233. https://doi.org/10.1029/2011JA017256

Hwang, K.-J., Kuznetsova, M. M., Sahraoui, F., Goldstein, M. L., Lee, E., & Parks, G. K. (2011). Kelvin-Helmholtz waves under southward interplanetary magnetic field. *Journal of Geophysical Research*, *116*(A15), 8210. https://doi.org/10.1029/2011JA016596

Hwang, K.-J., Wang, C.-P., Nykyri, K., Hasegawa, H., Tapley, M. B., Burch, J. L., et al. (2023). Kelvin-Helmholtz instability-driven magnetopause dynamics as turbulent pathway for the solar wind-magnetosphere coupling and the flank-central plasma sheet communication. *Frontiers in Astronomy and Space Sciences*, *10*, 1151869. https://doi.org/10.3389/fspas.2023.1151869

Jia, X., Hansen, K. C., Gombosi, T. I., Kivelson, M. G., Tóth, G., DeZeeuw, D. L., & Ridley, A. J. (2012). Magnetospheric configuration and dynamics of saturn's magnetosphere: A global MHD simulation. *Journal of Geophysical Research*, *117*(A5), 2012JA017575. https://doi.org/10.1029/2012JA017575

Johnson, J., Wing, S., & Delamere, P. (2014). Kelvin Helmholtz instability in planetary magnetospheres. *Space Science Reviews*, *184*(1–4), 1–31. https://doi.org/10.1007/s11214-014-0085-z

Johnson, J. R., & Wing, S. (2009). Northward interplanetary magnetic field plasma sheet entropies. *Journal of Geophysical Research: Space Physics*, *114*(A13). https://doi.org/10.1029/2008JA014017

Johnson, J. R., & Wing, S. (2015). The dependence of the strength and thickness of field-aligned currents on solar wind and ionospheric parameters. *Journal of Geophysical Research: Space Physics*, *120*(5), 3987–4008. https://doi.org/10.1002/2014JA020312

Johnson, J. R., Wing, S., Delamere, P., Petrinec, S., & Kavosi, S. (2021). Field-aligned currents in auroral vortices. *Journal of Geophysical Research: Space Physics*, *126*(2), e2020JA028583. https://doi.org/10.1029/2020JA028583

Joy, S. P., Kivelson, M. G., Walker, R. J., Khurana, K. K., Russell, C. T., & Ogino, T. (2002). Probabilistic models of the Jovian magnetopause and bow shock locations. *Journal of Geophysical Research*, *107*(A10), 1309. https://doi.org/10.1029/2001JA009146

Kanani, S. J., Arridge, C. S., Jones, G. H., Fazakerley, A. N., McAndrews, H. J., Sergis, N., et al. (2010). A new form of Saturn's magnetopause using a dynamic pressure balance model, based on in situ, multi-instrument Cassini measurements. *Journal of Geophysical Research: Space Physics*, *115*(A14), 6207. https://doi.org/10.1029/2009JA014262

Kavosi, S., & Raeder, J. (2015). Ubiquity of Kelvin-Helmholtz waves at earth's magnetopause. *Nature Communications*, *6*(1), 7019. https://doi.org/10.1038/ncomms8019

Kavosi, S., Raeder, J., Johnson, J. R., Nykyri, K., & Farrugia, C. J. (2023). Seasonal and diurnal variations of Kelvin-Helmholtz Instability at terrestrial magnetopause. *Nature Communications*, *14*(1), 2513. https://doi.org/10.1038/s41467-023-37485-x

Kavosi, S., Spence, H. E., Fennell, J. F., Turner, D. L., Connor, H. K., & Raeder, J. (2018). MMS/FEEPS observations of electron microinjections due to Kelvin-Helmholtz waves and flux transfer events: A case study. *Journal of Geophysical Research: Space Physics*, *123*(7), 5364–5378. https://doi.org/10.1029/2018JA025244

La Belle-Hamer, A. L., Otto, A., & Lee, L. C. (1995). Magnetic reconnection in the presence of sheared flow and density asymmetry: Applications to the Earth's magnetopause. *Journal of Geophysical Research*, *100*(A7), 11875–11889. https://doi.org/10.1029/94JA00969

Lammer, H., Lichtenegger, H., Biernat, H., Erkaev, N., Arshukova, I., Kolb, C., et al. (2006). Loss of hydrogen and oxygen from the upper atmosphere of Venus. *Planetary and Space Science*, *54*(13–14), 1445–1456. https://doi.org/10.1016/j.pss.2006.04.022

Leroy, M. H. J., Ripperda, B., & Keppens, R. (2019). Particle orbits at the magnetopause: Kelvin-Helmholtz induced trapping. *Journal of Geophysical Research: Space Physics*, *124*(8), 6715–6729. https://doi.org/10.1029/2019JA026994

Li, T., Li, W., Tang, B., Khotyaintsev, Y. V., Graham, D. B., Ardakani, A., et al. (2023). Kelvin-Helmholtz waves and magnetic reconnection at the earth's magnetopause under southward interplanetary magnetic field. *Geophysical Research Letters*, *50*(20), e2023GL105539. https://doi.org/10.1029/2023GL105539

Li, W., André, M., Khotyaintsev, Y. V., Vaivads, A., Graham, D. B., Toledo-Redondo, S., et al. (2016). Kinetic evidence of magnetic reconnection due to Kelvin-Helmholtz waves. *Geophysical Research Letters*, *43*(11), 5635–5643. https://doi.org/10.1002/2016GL069192

Li, W., Wang, C., Tang, B., Guo, X., & Lin, D. (2013). Global features of Kelvin-Helmholtz waves at the magnetopause for northward interplanetary magnetic field. *Journal of Geophysical Research: Space Physics*, *118*(8), 5118–5126. https://doi.org/10.1002/jgra.50498

Lin, D., Wang, C., Li, W., Tang, B., Guo, X., & Peng, Z. (2014). Properties of Kelvin-Helmholtz waves at the magnetopause under northward interplanetary magnetic field: Statistical study. *Journal of Geophysical Research: Space Physics*, *119*(9), 7485–7494. https://doi.org/10.1002/2014JA020379

Liu, Z. (2023). Slandarer (2023). 200 colormap [code]. *MATLAB Central File Exchange*. Retrieved from https://www.mathworks.com/matlabcentral/fileexchange/120088-200-colormap

Ma, X. (2023). Estimation of the Kelvin-Helmholtz unstable boundary. *Journal of Geophysical Research: Space Physics*, *128*(8), e2023JA031602. https://doi.org/10.1029/2023JA031602

Ma, X. (2024). Density and magnetic field asymmetric Kelvin-Helmholtz instability [Dataset]. figshare. https://doi.org/10.6084/m9.figshare.24418369.v1

Ma, X., Delamere, P., Nykyri, K., Burkholder, B., Eriksson, S., & Liou, Y.-L. (2021). Ion dynamics in the Meso-scale 3-D Kelvin-Helmholtz instability: Perspectives from test particle simulations. *Frontiers in Astronomy and Space Sciences*, *8*, 758442. https://doi.org/10.3389/fspas.2021.758442

Ma, X., Delamere, P., Otto, A., & Burkholder, B. (2017). Plasma transport driven by the three-dimensional Kelvin-Helmholtz instability. *Journal of Geophysical Research: Space Physics*, *122*(10), 10382–10395. https://doi.org/10.1002/2017JA024394

Ma, X., Delamere, P. A., Nykyri, K., Burkholder, B., Neupane, B., & Rice, R. C. (2019). Comparison between fluid simulation with test particles and hybrid simulation for the Kelvin-Helmholtz instability. *Journal of Geophysical Research: Space Physics*, *124*(8), 6654–6668. https://doi.org/10.1029/2019ja026890

21699402, 2024, 3, Downloaded from https://agupubs.onlinelibrary.wiley.com/doi/10.1029/2023JA032234, Wiley Online Library on [17/05/2024]. See the Terms and Conditions (https://onlinelibrary.wiley.com/terms-and-conditions) on Wiley Online Library for rules of use; OA articles are governed by the applicable Creative Commons License

Ma, X., Delamere, P. A., Schok, A., Wing, S., Johnson, J. R., & Liou, Y. (2022). Jupiter's sheared flow unstable magnetopause boundary observed by Juno. *Journal of Geophysical Research: Space Physics*, *127*(10). https://doi.org/10.1029/2022JA030719

Ma, X., Nykyri, K., Dimmock, A., & Chu, C. (2020). Statistical study of solar wind, magnetosheath, and magnetotail plasma and field properties: 12+ years of THEMIS observations and MHD simulations. *Journal of Geophysical Research: Space Physics*, *125*(10), e2020JA028209. https://doi.org/10.1029/2020JA028209

Ma, X., & Otto, A. (2013). Mechanisms of field-aligned current formation in magnetic reconnection. *Journal of Geophysical Research: Space Physics*, *118*(8), 4906–4914. https://doi.org/10.1002/jgra.50457

Ma, X., Otto, A., & Delamere, P. A. (2014a). Interaction of magnetic reconnection and Kelvin-Helmholtz modes for large magnetic shear: 1. Kelvin-Helmholtz trigger. *Journal of Geophysical Research: Space Physics*, *119*(2), 781–797. https://doi.org/10.1002/2013ja019224

Ma, X., Otto, A., & Delamere, P. A. (2014). Interaction of magnetic reconnection and kelvin-Helmholtz modes for large magnetic shear: 2. Reconnection trigger. *Journal of Geophysical Research: Space Physics*, *119*(2), 808–820. https://doi.org/10.1002/2013ja019225

Ma, X., Otto, A., Delamere, P. A., & Zhang, H. (2016). Interaction between reconnection and Kelvin-Helmholtz at the high-latitude magnetopause. *Advances in Space Research*, *58*(2), 231–239. https://doi.org/10.1016/j.asr.2016.02.025

Ma, X., Stauffer, B., Delamere, P. A., & Otto, A. (2015). Asymmetric Kelvin-Helmholtz propagation at Saturn's dayside magnetopause. *Journal of Geophysical Research: Space Physics*, *120*(3), 1867–1875. https://doi.org/10.1002/2014JA020746

Masters, A., Achilleos, N., Cutler, J., Coates, A., Dougherty, M., & Jones, G. (2012). Surface waves on Saturn's magnetopause. *Planetary and Space Science*, *65*(1), 109–121. https://doi.org/10.1016/j.pss.2012.02.007

Masters, A., Achilleos, N., Kivelson, M. G., Sergis, N., Dougherty, M. K., Thomsen, M. F., et al. (2010). Cassini observations of a Kelvin-Helmholtz vortex in Saturn's outer magnetosphere. *Journal of Geophysical Research*, *115*(A7), 2010JA015351. https://doi.org/10.1029/2010JA015351

Matsumoto, Y., & Hoshino, M. (2004). Onset of turbulence induced by a Kelvin-Helmholtz vortex: Onset of turbulence by a K-H vortex. *Geophysical Research Letters*, *31*(2). https://doi.org/10.1029/2003GL018195

Matsumoto, Y., & Hoshino, M. (2006). Turbulent mixing and transport of collisionless plasmas across a stratified velocity shear layer. *Journal of Geophysical Research*, *111*(A5), A05213. https://doi.org/10.1029/2004JA010988

Matsumoto, Y., & Seki, K. (2010). Formation of a broad plasma turbulent layer by forward and inverse energy cascades of the Kelvin-Helmholtz instability: Broad turbulent layer BY KH instability. *Journal of Geophysical Research*, *115*(A10). https://doi.org/10.1029/2009JA014637

Milan, S. E. (2004). Dayside and nightside contributions to the cross polar cap potential: Placing an upper limit on a viscous-like interaction. *Annales Geophysicae*, *22*(10), 3771–3777. https://doi.org/10.5194/angeo-22-3771-2004

Miller, K. L., Knudsen, W. C., & Spenner, K. (1984). The dayside Venus ionosphere. *Icarus*, *57*(3), 386–409. https://doi.org/10.1016/0019-1035(84)90125-8

Miura, A. (1984). Anomalous transport by magnetohydrodynamic Kelvin-Helmholtz instabilities in the solar wind-magnetosphere interaction. *Journal of Geophysical Research*, *89*(A2), 801–818. https://doi.org/10.1029/JA089iA02p00801

Miura, A., & Pritchett, P. L. (1982). Nonlocal stability analysis of the MHD Kelvin-Helmholtz instability in a compressible plasma. *Journal of Geophysical Research*, *87*(A9), 7431–7444. https://doi.org/10.1029/JA087iA09p07431

Montgomery, J., Ebert, R. W., Allegrini, F., Bagenal, F., Bolton, S. J., DiBraccio, G. A., et al. (2023). Investigating the occurrence of Kelvin-Helmholtz instabilities at Jupiter's dawn magnetopause. *Geophysical Research Letters*, *50*(14), e2023GL102921. https://doi.org/10.1029/2023GL102921

Moore, T. W., Nykyri, K., & Dimmock, A. P. (2016). Cross-scale energy transport in space plasmas. *Nature Physics*, *12*(12), 1164–1169. https://doi.org/10.1038/nphys3869

Moore, T. W., Nykyri, K., & Dimmock, A. P. (2017). Ion-scale wave properties and enhanced ion heating across the low-latitude boundary layer during Kelvin-Helmholtz instability. *Journal of Geophysical Research: Space Physics*, *122*(11), 11128–11153. https://doi.org/10.1002/2017JA024591

Möstl, U. V., Erkaev, N. V., Zellinger, M., Lammer, H., Gröller, H., Biernat, H. K., & Korovinskiy, D. (2011). The Kelvin–Helmholtz instability at Venus: What is the unstable boundary? *Icarus*, *216*(2), 476–484. https://doi.org/10.1016/j.icarus.2011.09.012

Nichols, J. D., Badman, S. V., Bagenal, F., Bolton, S. J., Bonfond, B., Bunce, E. J., et al. (2017). Response of Jupiter's auroras to conditions in the interplanetary medium as measured by the Hubble Space Telescope and Juno. *Geophysical Research Letters*, *44*(15), 7643–7652. https://doi.org/10.1002/2017GL073029

Nykyri, K., Chu, C., Ma, X., Fuselier, S. A., & Rice, R. (2019). First MMS observation of energetic particles trapped in high-latitude magnetic field depressions. *Journal of Geophysical Research: Space Physics*, *124*(1), 197–210. https://doi.org/10.1029/2018ja026131

Nykyri, K., & Foullon, C. (2013). First magnetic seismology of the CME reconnection outflow layer in the low corona with 2.5-D MHD simulations of the Kelvin-Helmholtz instability. *Geophysical Research Letters*, *40*(16), 4154–4159. https://doi.org/10.1002/grl.50807

Nykyri, K., Ma, X., Burkholder, B., Rice, R., Johnson, J. R., Kim, E., et al. (2021). MMS observations of the multiscale wave structures and parallel electron heating in the vicinity of the southern exterior cusp. *Journal of Geophysical Research: Space Physics*, *126*(3), e2019JA027698. https://doi.org/10.1029/2019ja027698

Nykyri, K., & Otto, A. (2001). Plasma transport at the magnetospheric boundary due to reconnection in Kelvin-Helmholtz vortices. *Geophysical Research Letters*, *28*(18), 3565–3568. https://doi.org/10.1029/2001GL013239

Nykyri, K., Otto, A., Adamson, E., Kronberg, E., & Daly, P. (2012). On the origin of high-energy particles in the cusp diamagnetic cavity. *Journal of Atmospheric and Solar-Terrestrial Physics*, *87*, 70–81. https://doi.org/10.1016/j.jastp.2011.08.012

Ofman, L., & Thompson, B. J. (2011). SDO/AIA observation of Kelvin-Helmholtz instability in the solar corona. *The Astrophysical Journal*, *734*(1), L11. https://doi.org/10.1088/2041-8205/734/1/L11

Otto, A. (1999). Three-dimensional magnetic reconnection in astrophysical plasmas—MHD approach. *Astrophysics and Space Science*, *264*(1/4), 17–24. https://doi.org/10.1023/a:1002499315748

Otto, A. (2006). December Mass transport at the magnetospheric flanks associated with three-dimensional Kelvin-Helmholtz modes. In *AGU fall meeting abstracts* (Vol. 2006). SM33B–0365.

Otto, A., & Fairfield, D. H. (2000). Kelvin-Helmholtz instability at the magnetotail boundary: MHD simulation and comparison with geotail observations. *Journal of Geophysical Research*, *105*(A9), 21175–21190. https://doi.org/10.1029/1999JA000312

Paral, J., & Rankin, R. (2013). Dawn–dusk asymmetry in the Kelvin–Helmholtz instability at Mercury. *Nature Communications*, *4*(1), 1645. https://doi.org/10.1038/ncomms2676

Poh, G., Espley, J. R., Nykyri, K., Fowler, C. M., Ma, X., Xu, S., et al. (2021). On the growth and development of non-linear Kelvin-Helmholtz instability at Mars: MAVEN observations. *Journal of Geophysical Research: Space Physics*, *126*(9). https://doi.org/10.1029/2021JA029224

Pope, S. A., Balikhin, M. A., Zhang, T. L., Fedorov, A. O., Gedalin, M., & Barabash, S. (2009). Giant vortices lead to ion escape from Venus and re-distribution of plasma in the ionosphere: Vortices at Venus. *Geophysical Research Letters*, *36*(7). https://doi.org/10.1029/2008GL036977

21699402, 2024, 3, Downloaded from https://agupubs.onlinelibrary.wiley.com/doi/10.1029/2023JA032234, Wiley Online Library on [17/05/2024]. See the Terms and Conditions (https://onlinelibrary.wiley.com/terms-and-conditions) on Wiley Online Library for rules of use; OA articles are governed by the applicable Creative Commons License

Ranquist, D. A., Bagenal, F., Wilson, R. J., Hospodarsky, G., Ebert, R. W., Allegrini, F., et al. (2019). Survey of Jupiter's dawn magnetosheath using Juno. *Journal of Geophysical Research: Space Physics*, *124*(11), 9106–9123. https://doi.org/10.1029/2019JA027382

Rice, R. C., Nykyri, K., Ma, X., & Burkholder, B. L. (2022). Characteristics of Kelvin-Helmholtz waves as observed by the MMS from September 2015 to March 2020. *Journal of Geophysical Research: Space Physics*, *127*(3). https://doi.org/10.1029/2021JA029685

Russell, C., Luhmann, J., & Strangeway, R. (2006). The solar wind interaction with Venus through the eyes of the Pioneer Venus Orbiter. *Planetary and Space Science*, *54*(13–14), 1482–1495. https://doi.org/10.1016/j.pss.2006.04.025

Schok, A. A., Delamere, P. A., Mino, B., Damiano, P. A., Zhang, B., Sciola, A., et al. (2023). Periodicities and plasma density structure of Jupiter's dawnside magnetosphere. *Journal of Geophysical Research: Planets*, *128*(2). https://doi.org/10.1029/2022JE007637

Swisdak, M., Rogers, B. N., Drake, J. F., & Shay, M. A. (2003). Diamagnetic suppression of component magnetic reconnection at the magnetopause. *Journal of Geophysical Research (Space Physics)*, *108*(A5), 1218. https://doi.org/10.1029/2002JA009726

Taylor, M. G. G. T., & Lavraud, B. (2008). Observation of three distinct ion populations at the Kelvin-Helmholtz-unstable magnetopause. *Annales Geophysicae*, *26*(6), 1559–1566. https://doi.org/10.5194/angeo-26-1559-2008

Terada, N., Machida, S., & Shinagawa, H. (2002). Global hybrid simulation of the Kelvin-Helmholtz instability at the Venus ionopause: K-H instability at Venus ionopause. *Journal of Geophysical Research*, *107*(A12). https://doi.org/10.1029/2001JA009224

Thomsen, M. F., Jackman, C. M., & Lamy, L. (2019). Solar wind dynamic pressure upstream from Saturn: Estimation from magnetosheath properties and comparison with SKR. *Journal of Geophysical Research: Space Physics*, *124*(10), 7799–7819. https://doi.org/10.1029/2019JA026819

Thomsen, M. F., Reisenfeld, D. B., Delapp, D. M., Tokar, R. L., Young, D. T., Crary, F. J., et al. (2010). Survey of ion plasma parameters in Saturn's magnetosphere: Plasma in Saturn's magnetosphere. *Journal of Geophysical Research*, *115*(A10). https://doi.org/10.1029/2010JA015267

Vasyliunas, V. M. (1984). Fundamentals of current description. In T. A. Potemra (Ed.), *American geophysical union geophysical monograph series* (Vol. 28, pp. 63–66). https://doi.org/10.1029/GM028p0063

Walker, S. N., Balikhin, M. A., Zhang, T. L., Gedalin, M. E., Pope, S. A., Dimmock, A. P., & Fedorov, A. O. (2011). Unusual nonlinear waves in the Venusian magnetosheath: Dayside Venusian vortices. *Journal of Geophysical Research*, *116*(A1). https://doi.org/10.1029/2010JA015916

Walsh, B. M., Thomas, E. G., Hwang, K.-J., Baker, J. B. H., Ruohoniemi, J. M., & Bonnell, J. W. (2015). Dense plasma and Kelvin-Helmholtz waves at Earth's dayside magnetopause. *Journal of Geophysical Research: Space Physics*, *120*(7), 5560–5573. https://doi.org/10.1002/2015JA021014

Walsh, B. M., Welling, D. T., Zou, Y., & Nishimura, Y. (2018). A maximum spreading speed for magnetopause reconnection. *Geophysical Research Letters*, *45*(11), 5268–5273. https://doi.org/10.1029/2018GL078230

Wilder, F. D., King, A., Gove, D., Eriksson, S., Ahmadi, N., Workman, T. L., et al. (2023). The occurrence and prevalence of magnetic reconnection in the Kelvin-Helmholtz instability under various solar wind conditions. *Journal of Geophysical Research: Space Physics*, *128*(10), e2023JA031583. https://doi.org/10.1029/2023JA031583

Wing, S., & Johnson, J. R. (2015). Theory and observations of upward field-aligned currents at the magnetopause boundary layer. *Geophysical Research Letters*, *42*(21), 9149–9155. https://doi.org/10.1002/2015GL065464

Yan, G. Q., Mozer, F. S., Parks, G. K., Cai, C. L., Chen, T., Goldstein, M. L., & Ren, Y. (2022). Substructure of a Kelvin-Helmholtz vortex accompanied by plasma transport under the northward interplanetary magnetic field. *Journal of Geophysical Research: Space Physics*, *127*(2), e2021JA029735. https://doi.org/10.1029/2021JA029735

Yan, G. Q., Mozer, F. S., Shen, C., Chen, T., Parks, G. K., Cai, C. L., & McFadden, J. P. (2014). Kelvin-Helmholtz vortices observed by THEMIS at the duskside of the magnetopause under southward interplanetary magnetic field. *Geophysical Research Letters*, *41*(13), 4427–4434. https://doi.org/10.1002/2014GL060589

Yan, G. Q., Parks, G. K., Mozer, F. S., Goldstein, M. L., Chen, T., & Liu, Y. (2023). Rayleigh-taylor instability observed at the dayside magnetopause under northward interplanetary magnetic field. *Journal of Geophysical Research: Space Physics*, *128*(7), e2023JA031461. https://doi.org/10.1029/2023JA031461

Zhang, B., Delamere, P., Ma, X., Burkholder, B., Wiltberger, M., Lyon, J., et al. (2018). Asymmetric Kelvin-Helmholtz instability at Jupiter's magnetopause boundary: Implications for corotation-dominated systems. *Geophysical Research Letters*, *45*(1), 56–63. https://doi.org/10.1002/2017gl076315

Zhang, T., Delva, M., Baumjohann, W., Volwerk, M., Russell, C., Barabash, S., et al. (2008). Initial Venus Express magnetic field observations of the magnetic barrier at solar minimum. *Planetary and Space Science*, *56*(6), 790–795. https://doi.org/10.1016/j.pss.2007.10.013

Zou, Y., Walsh, B. M., Nishimura, Y., Angelopoulos, V., Ruohoniemi, J. M., McWilliams, K. A., & Nishitani, N. (2018). Spreading speed of magnetopause reconnection X-lines using ground-satellite coordination. *Geophysical Research Letters*, *45*(1), 80–89. https://doi.org/10.1002/2017GL075765

Zou, Y., Walsh, B. M., Nishimura, Y., Angelopoulos, V., Ruohoniemi, J. M., McWilliams, K. A., & Nishitani, N. (2019). Local time extent of magnetopause reconnection using space–ground coordination. *Annales Geophysicae*, *37*(2), 215–234. https://doi.org/10.5194/angeo-37-215-2019

21699402, 2024, 3, Downloaded from https://agupubs.onlinelibrary.wiley.com/doi/10.1029/2023JA032234, Wiley Online Library on [17/05/2024]. See the Terms and Conditions (https://onlinelibrary.wiley.com/terms-and-conditions) on Wiley Online Library for rules of use; OA articles are governed by the applicable Creative Commons License